Detecting axion dark matter with Rydberg atoms via induced electric dipole transitions

Georg Engelhardt [1,2,3,*] Amit Bhoonah,[4,†] and W. Vincent Liu [4,2,5,‡]

[1] *Shenzhen Institute for Quantum Science and Engineering, Southern University of Science and Technology, Shenzhen 518055, China*
[2] *International Quantum Academy–Shenzhen, Shenzhen 518048, China*
[3] *Guangdong Provincial Key Laboratory of Quantum Science and Engineering, Southern University of Science and Technology, Shenzhen 518055, China*
[4] *Department of Physics and Astronomy and IQ Initiative, University of Pittsburgh, Pittsburgh, Pennsylvania 15260, USA*
[5] *Shanghai Research Center for Quantum Sciences, Shanghai 201315, China*

(Received 13 October 2023; accepted 2 February 2024; published 4 April 2024)

Long-standing efforts to detect axions are driven by two compelling prospects, naturally accounting for the absence of charge-conjugation and parity symmetry breaking in quantum chromodynamics, and for the elusive dark matter at ultralight mass scale. Many experiments use advanced cavity resonator setups to probe the magnetic-field-mediated conversion of axions to photons. Here, we show how to search for axion matter without relying on such a cavity setup, which opens a new path for the detection of ultralight axions, where cavity-based setups are infeasible. When applied to Rydberg atoms, which feature particularly large transition dipole elements, this effect promises an outstanding sensitivity for detecting ultralight dark matter. Our estimates show that it can provide laboratory constraints in parameter space that so far have only been probed astrophysically, and cover new unprobed regions of the parameter space. The Rydberg atomic gases offer a flexible and inexpensive experimental platform that can operate at room temperature. We project the sensitivity by quantizing the axion-modified Maxwell equations to accurately describe atoms and molecules as quantum sensors wherever axion dark matter is present.

DOI: 10.1103/PhysRevResearch.6.023017

I. INTRODUCTION

There is overwhelming astrophysical and cosmological evidence that approximately 85% of matter in the universe is in the form of nonluminous *dark matter*. Unfortunately, little is known about its nature beyond its gravitational influence on galactic and cosmological scales. While the search for historically popular models like weakly interacting massive particles (WIMPs) continues, it is important to expand experimental efforts to other well-motivated candidates. One such class of models, ultralight bosonic dark matter, is particularly favored because of discrepancies that arise when simulations of structure formation with WIMP-like dark matter are compared to observations on galactic scales [1–3]. These tensions are somewhat alleviated when the dark matter is modeled not as a WIMP-like particle but as an ultralight boson with de Broglie wavelength comparable to small-scale galactic structures, which corresponds to a mass of order 10^{-21} eV$/c^2$.

The axion is a famous candidate of bosonic dark matter, which was originally predicted as the symmetry consequence of the Peccei-Quinn model as new physics beyond the standard model of elementary particle physics [4–7]. It provides a "missing" elementary particle capable of naturally explaining why the charge-conjugation and parity symmetry (CP) are preserved in quantum chromodynamics (QCD) but are known to be violated in the electroweak interaction. This crucial conundrum has been coined the "strong CP" problem in elementary particle physics. While these *QCD axions* may be the dark matter [8–10], it is possible that the latter are pseudoscalars, which, however, do not solve the strong charge-parity problem. To distinguish them from the *QCD axion*, such pseudoscalars are called axionlike particles, and they can usually be searched for with the same tools and techniques used to probe QCD axions. For the remainder of this article, we will use "axion" to refer to a dark-matter candidate regardless of whether it solves the strong CP problem or not whenever the distinction is unimportant. It is interesting to note that, aside from their key role in high-energy physics, axions have also been predicted to exist in condensed-matter systems [11–16] where they manifest in the form of magnetoelectric transport effects. Thus, a discovery of the axion will have important implications for the strong CP problem in QCD and the search for dark matter, potentially solving both problems simultaneously [17]. We will focus on the latter aspect in this work.

The axion-modified Maxwell equations predict that a magnetic field converts axions of energy $\hbar\omega_\text{a} \simeq m_\text{a}c^2 + \frac{1}{2}m_\text{a}v^2$ (mass m_a, velocity v) into photons of frequency ω_a as sketched in Fig. 1(a) [7]. As even the order of magnitude of the axion mass is unknown, the search for this hypothetical particle

*engelhardt@sustech.edu.cn
†amit.bhoonah@pitt.edu
‡wvliu@pitt.edu

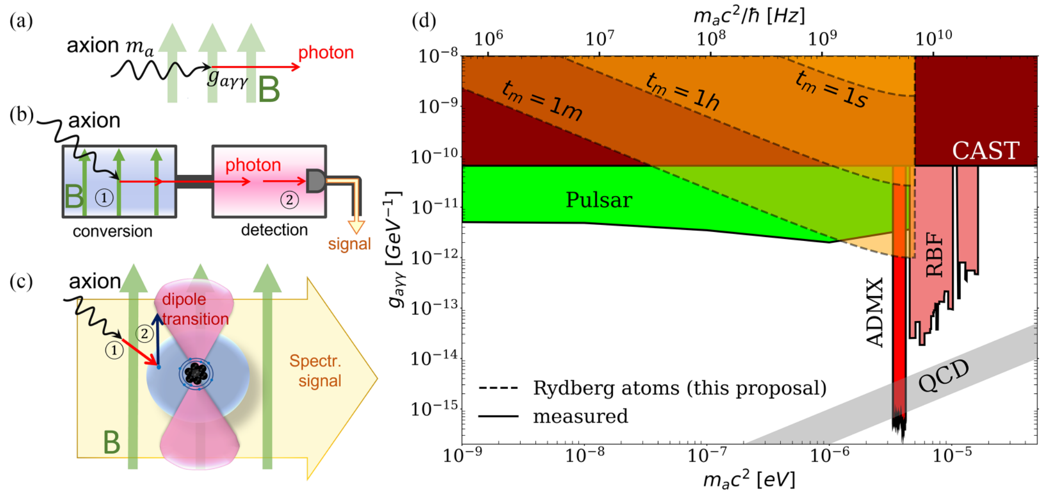

FIG. 1. (a) Magnetic-field-meditated axion-photon conversion. (b) Typical resonator-based setup for the detection of axion dark matter. (c) Illustration of the axion-induced electric dipole transition in an atom mediated by a magnetic field. The dipole transitions can be detected spectroscopically. (d) Overview of the exclusion boundaries for m_a and $g_{a\gamma\gamma}$. Experimentally excluded regions are marked by a solid line. The projected exclusion bounds using axion-induced dipole transitions in Rydberg atoms achievable within 1 s, 1 h, and 1 month measurement time are outlined by dashed lines. Also shown are constraints from the CERN Axion Solar Telescope (CAST) [18], and resonant axion-photon conversion around pulsars [19]. Other constraints shown in the plot for axions of a higher mass are from ADMX [20] and RBF-UF [21].

seems to remain an outstanding, long-lasting task. A typical experimental setup exploiting this resonant axion-photon conversion for the detection of the galactic axion field consists of two inductively coupled microwave resonators as depicted in Fig. 1(b) [22]. A microwave photon, sourced by the axion field in the first resonator, is detected in the second resonator using a SQUID device, Rydberg atoms, or comparable single-photon detectors. The RBF-UF [21], ADMX [20], and HAYSTAC [23–25] experiments attempt to detect the axion field in the narrow 1–200 μeV mass range to which they are limited by construction. It should not be surprising then that most constraints on axions in the mass regime $m_a c^2 < 2$ μeV are astrophysical or cosmological, such as using the Planck Telescope [26], Pulsar Timing Arrays (PTAs) [27], radio astronomy [28–30], spectroscopy from the Chandra X Ray Telescope [31], or observations of galaxy clusters [32,33]. However, while astrophysical systems offer volumes and exposure times, and sometimes energies, unattainable by terrestrial systems, they come with inherent uncertainties due to their complex nature. This makes complementary laboratory tests of experimental results derived from astrophysical systems invaluable. Current approaches, e.g., ABRACADBRA [34], ADMX SLIC [35], and SHAFT [36] using lumped-element circuits to compensate for the frequency mismatch, lose sensitivity as the mass of the axion is lowered [37]. Higher sensitivities have been theoretically proposed using electric sensing approaches [38] and twisted cavity resonators [39]. Notably, a resonant cavity for the detection of ultralight axions would be comparable in size to a small galaxy.

In this article, we analyze the possibility to search for the ultralight galactic axion field without relying on an advanced cavity resonator setup. Based on a rigorous quantization of the axion-Maxwell equations, which were first derived in their classical form by Sikivie in 1983 [40,41], and later proposed for advanced axion-electrodynamics in condensed-matter systems by Wilczek in 1987 [7], we derive an effective Hamiltonian that describes dipole transitions induced by the axion-sourced electric field as sketched in Fig. 1(c). Thus, highly sensitive electric field detectors using quantum emitters and spectroscopic methods can be easily repurposed for the search of axion dark matter.

The axion-induced dipole transitions are particularly well suited to Rydberg states which feature long lifetimes, large electric dipole moments, and polarizability [42]. Being quantum sensors, Rydberg atoms can take advantage of quantized energy levels, quantum coherence, or many-body entanglement to enhance detection sensitivity compared to classical systems [43]. Their aforementioned properties make them excellent candidates for electric field metrology in the radiofrequency regime, allowing sensitivities up to $\mu\mathrm{V m}^{-1}/\sqrt{\mathrm{Hz}}$ [44–48].

After introducing the axion-sourced electric field, we proceed to estimate the sensitivity of Rydberg atoms in a superheterodyne (superhet) detection configuration. For measurement campaigns over a period between seconds to months, we project constraints in the ultralight mass regime that can outperform existing exclusion limits [see Fig. 1(d)].

This article is organized as follows: In Sec. II A, we rigorously quantize the axion-Maxwell equations and derive an effective Hamiltonian that is convenient for a spectroscopic analysis. In Sec. III, we calculate the exclusion boundaries for axion dark matter for a superhet detector based on Rydberg atoms. In Sec. IV, we discuss conclusions and future improvements of our approach. Details of the derivations can be found in the Appendixes.

II. MICROSCOPIC DERIVATION OF THE HAMILTONIAN

To build our experimental proposal on a solid theoretical footing, we first accurately quantize the axion-Maxwell equations. Subsequently, we bring the quantized Hamiltonian into a suitable form for a sound spectroscopic analysis by deriving an effective Hamiltonian describing the interaction of the axion field with the quantum emitters (e.g., Rydberg atoms) in a microscopic fashion.

A. Quantization of the axion Maxwell equations

The axion field, being a pseudoscalar, interacts with the electric and magnetic fields via the Lagrangian term $\mathcal{L} = -g_{a\gamma\gamma}\sqrt{\frac{\epsilon_0}{\mu_0}}a\boldsymbol{E}\cdot\boldsymbol{B}$, where $\boldsymbol{E}, \boldsymbol{B}$, and a denote the classical electric, magnetic, and axion fields, respectively, which interact via a coupling constant $g_{a\gamma\gamma}$. The constants ϵ_0 and μ_0 denote the vacuum permittivity and permeability. The axion field is measured in units of eV and the interaction constant $g_{a\gamma\gamma}$ in units of $(\mathrm{eV})^{-1}$.

After deriving the Euler-Lagrange equations, one obtains the axion-Maxwell equations [7,40,41]

$$\nabla\cdot\boldsymbol{E} = \frac{\rho}{\epsilon_0} - cg_{a\gamma\gamma}\boldsymbol{B}\cdot\nabla a, \tag{1}$$

$$\nabla\times\boldsymbol{B} - \frac{\dot{\boldsymbol{E}}}{c^2} = \mu_0\boldsymbol{J} + \frac{g_{a\gamma\gamma}}{c}(\boldsymbol{B}\dot{a} - \boldsymbol{E}\times\nabla a), \tag{2}$$

$$\nabla\cdot\boldsymbol{B} = \boldsymbol{0}, \tag{3}$$

$$\nabla\times\boldsymbol{E} + \dot{\boldsymbol{B}} = \boldsymbol{0}, \tag{4}$$

$$\ddot{a} - c^2\nabla^2 a + \frac{m_a^2c^4}{\hbar^2}a = \hbar c^3\sqrt{\frac{\epsilon_0}{\mu_0}}g_{a\gamma\gamma}\boldsymbol{E}\cdot\boldsymbol{B}, \tag{5}$$

where $\boldsymbol{J}$ is the electric current density. Clearly, these equations reduce to the common Maxwell equations for $g_{a\gamma\gamma} = 0$.

The quantization of the axion-Maxwell equations follows essentially the same lines as the quantization of the common Maxwell equations, yet with replacing the electric field by

$$\hat{\boldsymbol{E}} = \hat{\boldsymbol{E}}_c - cg_{a\gamma\gamma}\hat{a}\hat{\boldsymbol{B}}, \tag{6}$$

where $\hat{\boldsymbol{E}}_c$ denotes the canonical electric field. The quantization procedure reveals that the canonical electric field fulfills canonical commutation relations rather than the actual physical electric field, which justifies its name. As we show in detail in Appendix A, the canonically quantized axion-light-matter Hamiltonian reads

$$\begin{aligned}\hat{H} =& \frac{1}{2}\int d^3\boldsymbol{r}\left[\epsilon_0\hat{\boldsymbol{E}}_c^{\perp 2} + \frac{1}{\mu_0}\hat{\boldsymbol{B}}^2\right]\\ &-\int d^3\boldsymbol{r}\left[\sqrt{\frac{\epsilon_0}{\mu_0}}g_{a\gamma\gamma}\hat{a}\hat{\boldsymbol{E}}_c\cdot\hat{\boldsymbol{B}} - \frac{1}{2\mu_0}(g_{a\gamma\gamma}\hat{a})^2\hat{\boldsymbol{B}}\cdot\hat{\boldsymbol{B}}\right]\\ &+\frac{1}{2}\int d^3\boldsymbol{r}\left[\frac{\hat{\pi}^2}{\hbar c^3} + \frac{1}{c\hbar}\nabla\hat{a}\cdot\nabla\hat{a} + \frac{m_a^2c^4}{c^3\hbar^3}\hat{a}^2\right]\\ &+\sum_\eta\left[\frac{\hat{\boldsymbol{p}}_\eta^2}{2m_\eta} + \frac{q_\eta^2}{2m_\eta c^2}\hat{\boldsymbol{A}}^2(\hat{\boldsymbol{r}}_\eta)\right]\\ &+\frac{1}{2}d^3\boldsymbol{r}\,[\hat{\rho}\hat{\phi} + \hat{\boldsymbol{J}}\cdot\hat{\boldsymbol{A}}],\end{aligned} \tag{7}$$

where the canonical electric field operator has been distributed in the transversal and longitudinal fields $\hat{\boldsymbol{E}}_c = \hat{\boldsymbol{E}}_c^\perp + \hat{\boldsymbol{E}}_c^\parallel$. The transversal contribution is defined by $\nabla\cdot\hat{\boldsymbol{E}}_c^\perp = \boldsymbol{0}$, while the longitudinal contribution is given by $\hat{\boldsymbol{E}}_c^\parallel = \hat{\boldsymbol{E}}_c - \hat{\boldsymbol{E}}_c^\perp = -\nabla\hat{\phi}$, where $\hat{\phi}$ is the common electrostatic potential. The vector potential and the magnetic field operators are denoted by $\hat{\boldsymbol{A}}$ and $\hat{\boldsymbol{B}}$, respectively. The axion field is denoted by $\hat{a}$, and $\hat{\pi}$ denotes its conjugated momentum. Particles with charge q_η and mass m_η at positions $\hat{\boldsymbol{r}}_\eta$ having momentum $\hat{\boldsymbol{p}}_\eta$ are labeled by $\eta \in \{1, \dots, N_p\}$. The coupling between light and matter reflects the minimal coupling principle. The field operators are quantized as

$$\hat{\rho}(\boldsymbol{r}) = \sum_{\eta=1}^{N_p} q_\eta\delta(\boldsymbol{r} - \hat{\boldsymbol{r}}_\eta), \tag{8}$$

$$\hat{\boldsymbol{J}}(\boldsymbol{r}) = \sum_{\eta=1}^{N_p} q_\eta\dot{\hat{\boldsymbol{r}}}_\eta\delta(\boldsymbol{r} - \hat{\boldsymbol{r}}_\eta) + \text{H.c.}, \tag{9}$$

$$\hat{\boldsymbol{A}}(\boldsymbol{r}) = \sum_{\boldsymbol{k},\lambda}\boldsymbol{e}_{\boldsymbol{k},\lambda}\sqrt{\frac{\hbar}{2\omega_{\boldsymbol{k}}\epsilon_0 V}}(\hat{d}_{\boldsymbol{k},\lambda}^\dagger e^{i\boldsymbol{k}\cdot\boldsymbol{r}} + \hat{d}_{\boldsymbol{k},\lambda}e^{-i\boldsymbol{k}\cdot\boldsymbol{r}}), \tag{10}$$

$$\hat{\boldsymbol{E}}_c^\perp(\boldsymbol{r}) = i\sum_{\boldsymbol{k},\lambda}\boldsymbol{e}_{\boldsymbol{k},\lambda}\sqrt{\frac{\hbar\omega_{\boldsymbol{k}}}{2\epsilon_0 V}}(\hat{d}_{\boldsymbol{k},\lambda}^\dagger e^{i\boldsymbol{k}\cdot\boldsymbol{r}} - \hat{d}_{\boldsymbol{k},\lambda}e^{-i\boldsymbol{k}\cdot\boldsymbol{r}}), \tag{11}$$

$$\hat{\boldsymbol{E}}_c^\parallel(\boldsymbol{r}) = -\nabla\hat{\phi}(\boldsymbol{r}),$$

$$\hat{\phi}(\boldsymbol{r}) = \frac{1}{4\pi\epsilon_0}\sum_{\eta=1}^{N_p}\frac{q_\eta}{|\boldsymbol{r} - \hat{\boldsymbol{r}}_\eta|}, \tag{12}$$

$$\hat{\boldsymbol{B}}(\boldsymbol{r}) = i\sum_{\boldsymbol{k},\lambda}\sqrt{\frac{\hbar}{2\omega_{\boldsymbol{k}}\epsilon_0 V}}(\boldsymbol{k}\times\boldsymbol{e}_{\boldsymbol{k},\lambda})(\hat{d}_{\boldsymbol{k},\lambda}^\dagger e^{i\boldsymbol{k}\cdot\boldsymbol{r}} - \hat{d}_{\boldsymbol{k},\lambda}e^{-i\boldsymbol{k}\cdot\boldsymbol{r}}). \tag{13}$$

The photonic operators $\hat{d}_{\boldsymbol{k},\lambda}$, which fulfill the canonical commutation relations and quantize the electromagnetic field, are labeled by wave vector $\boldsymbol{k}$ and polarization $\lambda \in \{\updownarrow, \leftrightarrow\}$. The frequencies of the photonic modes are given by $\omega_{\boldsymbol{k}}$. The quantization volume is denoted by V. The unit vectors $\boldsymbol{e}_{\boldsymbol{k},\lambda}$ describe the direction of polarization and are perpendicular to the wave vector, i.e., $\boldsymbol{e}_{\boldsymbol{k},\lambda}\cdot\boldsymbol{k} = \boldsymbol{0}$. This fact readily ensures that the electric and magnetic Gauss equations in Eqs. (1) and (3) are fulfilled. Using the Heisenberg equations of motion and the relation between canonical and physical electric fields in Eq. (6), we can derive the axion-Maxwell equations (1)–(5) in the classical limit by generalizing the derivation of the common Maxwell equations [49].

B. Axion-sourced electric field

It is inconvenient to proceed with the minimal-coupling Hamiltonian in Eq. (7), in particular, because of the appearance of the vector potential $\hat{\boldsymbol{A}}(\boldsymbol{r})$, which is not a physical observable. As the theoretical treatment of spectroscopy is usually performed in terms of the multipolar Hamiltonian [49], in which the matter directly couples to the electromagnet field, we transform the axion-light-matter Hamiltonian in Eq. (7) into the multipolar form by means of the Power-Zienau transformation [50]. In doing so, we introduce the canonical displacement field

$$\hat{\boldsymbol{D}}_c(\boldsymbol{r}) = \epsilon_0\hat{\boldsymbol{E}}_c(\boldsymbol{r}) + \hat{\boldsymbol{P}}(\boldsymbol{r}), \tag{14}$$

which is sourced only by the density of free charges ρ_{free} in the electric Gauss equation, i.e., $\nabla\cdot\hat{\boldsymbol{D}}_c = \rho_{\text{free}}$. The electric field sourced by the bounded charges is described by the polarization density $\hat{\boldsymbol{P}}(\boldsymbol{r})$. Details of this derivation can be found in Appendix B. The displacement field can be understood as the electromagnetic field in the absence of matter and describes thus an external electric field or the quantized electric field in a cavity. The polarization density describes the electric field generated by the matter.

To allow for a simple spectroscopic analysis, we derive an effective Hamiltonian in which the axion-field couples directly to the matter system. To this end, we envision an experimental setup with a strong static magnetic field, such that the total magnetic field operator can be distributed as $\hat{\boldsymbol{B}} = \boldsymbol{B} + \hat{\boldsymbol{B}}_{\mathrm{f}}$, where $\hat{\boldsymbol{B}}$ denotes the mean magnetic field and $\boldsymbol{B}_{\mathrm{f}}$ the quantum fluctuations. Likewise, we assume a macroscopically occupied axion mean field $\hat{a} \to a(t)$ as hypothesized for the galactic halo [51]. Calculating the dynamics of the electromagnetic fields in lowest order perturbation in $g_{\mathrm{a}\gamma\gamma} a(t)$, we arrive at an externally driven matter Hamiltonian, in which the axion field directly couples to the polarization $\hat{\boldsymbol{P}}(\boldsymbol{r})$. Details of this calculation are provided in Appendix C, where the externally driven matter Hamiltonian is given in Eq. (C20).

Let us consider an ensemble of N quantum emitters and denote their eigenstates by $|i, \mu\rangle$, where i labels the quantum emitter, and μ represents the collective electronic, vibrational, and rotational quantum numbers. In the dipole approximation, the polarization density operator can be expressed in terms of the eigenstates as

$$\hat{\boldsymbol{P}}(\boldsymbol{r}) = \sum_{i=1}^{N} \sum_{\mu,\nu} \boldsymbol{d}_{\mu,\nu}^{(i)} |i, \mu\rangle\langle i, \nu| \delta(\boldsymbol{r} - \boldsymbol{r}_i), \tag{15}$$

where $\delta(\boldsymbol{r})$ is the three-dimensional delta function, $\boldsymbol{r}_i$ is the position of the ith quantum emitter, and $\boldsymbol{d}_{\mu,\nu}^{(i)}$ is the transition dipole moment between the two eigenstates μ and ν. In doing so, we can describe the interaction of the axion field and the quantum emitters by means of the effective Hamiltonian

$$\hat{H}_{\text{a-d}} = -\sum_{i=1}^{N} \boldsymbol{E}_{\mathrm{a}}(t) \cdot \boldsymbol{d}_{\mu,\nu}^{(i)} |i, \mu\rangle\langle i, \nu|, \tag{16}$$

where we have introduced the effective axion-sourced electric field

$$\boldsymbol{E}_{\mathrm{a}}(t) = g_{\mathrm{a}\gamma\gamma} c a(t) \boldsymbol{B} \mathcal{S}\left(\frac{m_{\mathrm{a}} c}{\hbar} l_B\right). \tag{17}$$

The form function $\mathcal{S}(x)$ takes the spatial dynamics of the axion-sourced electric field into account. The exact form of $\mathcal{S}(x)$ depends on experimental details, such as the shape of the magnetic field, or the presence of a Faraday cage. Its unitless argument x is a product of the axion mass m_{a} and the length scale l_B of the magnetic field. For small arguments, it scales with $\mathcal{S}(x) \propto x^2$ for a spatially confined magnetic field in the absence of free charges, i.e., the sourced electric field is suppressed for small axion masses, constituting the main challenge to detect ultralight axions. In this work, we assume $\mathcal{S}(x) = x^2$ and a magnetic field length scale of $l_B = 0.1$ m.

Relation (17) implies that one can repurpose sensitive atomic and molecular detectors of electric fields to search for axion dark matter. The (classical) magnetic field can be considered as an experimental switch controlling the effective interaction strength between the axion field and the quantum emitters. This allows us to distinguish between a possible axion signal and background electric fields.

III. RYDBERG ATOMS AS AXION DETECTORS

A. Exclusion boundaries

Ultralight axions in the galactic halo exhibit wavelike behavior and must be treated as a classical time-varying background field [51], $a(t) = a_0 \cos(\omega_{\mathrm{a}} t + \phi_{\mathrm{a}})$, where a_0 is the amplitude of the axion field, ϕ_{a} is its phase, and $\hbar\omega_{\mathrm{a}} \simeq m_{\mathrm{a}} c^2 + \frac{1}{2} m_{\mathrm{a}} v^2$ is its energy. Since the field has a small frequency dispersion described by the dark matter velocity distribution (average value $10^{-3}c$), a coherence time can be estimated to be $\tau_C = \frac{2\hbar}{m_{\mathrm{a}} c^2} 10^6$, which defines the time scale over which the phase ϕ_a can be considered to be constant [52,53]. For axions in the ultralight mass regime, this timescale will always be much larger than the measurement time in question. The amplitude a_0 can be estimated via the galactic dark-matter energy density $\rho = (m_{\mathrm{a}}^2 c^4 a_0^2)/(2\hbar^3 c^3) = 0.3 \times 10^{15}\ \frac{\mathrm{eV}}{\mathrm{m}^3}$. Solving Eq. (17) for $g_{\mathrm{a}\gamma\gamma}$, we find that the sensitivity for the interaction parameter is given by

$$g_{\mathrm{a}\gamma\gamma,*} = \frac{|\boldsymbol{E}_*|}{c|\boldsymbol{B}|} \sqrt{\frac{\hbar}{2\rho c^3 m_{\mathrm{a}}^2 l_B^4}}, \tag{18}$$

which assumes that axions constitute 100% of the dark matter in the universe.

Equation (16) shows that atoms with large transition dipole moments, in particular Rydberg states, couple strongly to the axion field. Using an advanced electromagnetically induced transparency (EIT) based superhet detection protocol, an electric field of $|\boldsymbol{E}_*| = 78 \times 10^{-9}$ V m^{-1} could be detected within 5000 s measurement time [44]. Taking this setup as the basis for our sensitivity projection, we estimate that $N = 10^4$ Rydberg atoms are able to detect minimal electric fields of $|\boldsymbol{E}_*| = 30 \times 10^{-9}$, 500×10^{-12}, and 18×10^{-12} V m^{-1} within a measurement time of $t_{\mathrm{m}} = 1$ s, 1 h, and 1 month, respectively, under ideal conditions.

Taking these values for reference, Fig. 1(d) shows the projected minimal detectable $g_{\mathrm{a}\gamma\gamma,*}$ evaluated via Eq. (18) for a magnetic field of $|\boldsymbol{B}| = 5.6$ T. It can be readily seen that Rydberg atoms can compete with the CAST helioscope bounds [18] in the mass regime $m_{\mathrm{a}} c^2 = (5 \times 10^{-8}) - (5 \times 10^{-6})$ eV. Also shown in the same plot are constraints inferred from the resonant axion-photon conversion around pulsars [19]. Rydberg atoms can thus set new leading experimental constraints while being operationally simple to realize. Due to their level structure, Rydberg atoms are particular sensitive in the small frequency regime. Their electric-field sensitivity is thereby relatively independent of the frequency for $\omega < 10$ GHz. The exclusion bound established by the Rydberg atoms scales thus with $g_{\mathrm{a}\gamma\gamma} \propto m_{\mathrm{a}}^{-1}$, as the suppression factor in Eq. (17) scales with $\propto m_{\mathrm{a}}^2$ and the axion field amplitude with $\propto m_{\mathrm{a}}^{-1}$. For larger masses $m_{\mathrm{a}} c^2 > 5 \times 10^{-6}$ eV, Rydberg atoms perform significantly worse than the ADMX [20], and RBF-UF [21] experiments, whose frequency regimes allows to amplify the axion-sourced electric field in a resonator setup prior to detection.

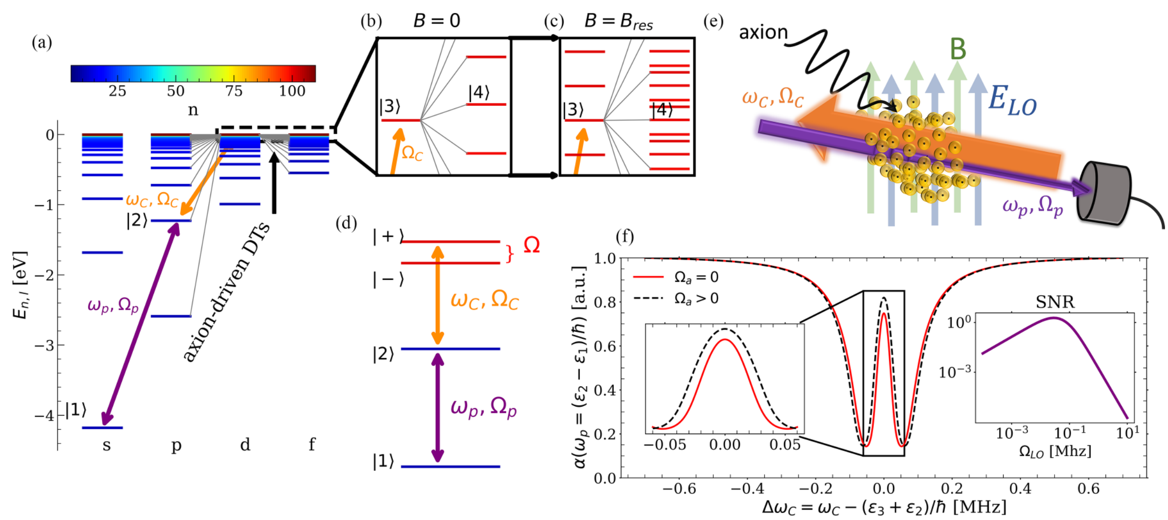

FIG. 2. (a) Energy levels of a rubidium atom for $n \geqslant 5$ resolved for the angular momentum orbitals s, p, d, f. Part (b) depicts a magnification of highly excited f orbitals that are coupled to the Rydberg level $|3\rangle$ with quantum numbers $n = 100$ and $l = 2$ (d orbital). Part (c) is the same as (b), but for a finite external magnetic field $B = B_{\rm res}$, which establishes a resonance condition between levels $|3\rangle$ with $(n, l, j, m) = (100, 2, 3/2, 1/2)$ and $|4\rangle$ with $(n, l, j, m) = (99, 3, 5/2, 1/2)$. Gray lines depict the allowed dipole transitions for a linearly polarized driving field. (d) Effective four-level system considered in the description of the Rydberg-atom superheterodyne detector. Levels $|-\rangle$ and $|+\rangle$ appear upon coupling the states $|3\rangle$ and $|4\rangle$. (e) Sketch of the spectroscopic setup, in which the probe and coupling fields propagate in the opposite direction to mitigate the Doppler effect as explained in Appendix D 7. (f) Absorption rate $\alpha(\omega_p)$ of the probe beam as a function of $\Delta\omega_{\rm C} = \omega_{\rm C} - (\epsilon_3 + \epsilon_2)/\hbar$ at resonance $\hbar\omega_p = \epsilon_2 - \epsilon_1$. The left inset depicts the absorption rate for small $|\Delta\omega_{\rm C}| \lesssim \gamma$. The right inset depicts the signal-to-noise ratio (SNR) as a function of the local oscillator $\Omega_{\rm LO}$ at $\Delta\omega_{\rm C} = 0$. Other parameters are $\Omega_p = 1.7$ MHz, $\Omega_{\rm C} = 23$ MHz, $B_{\rm res} = 5.6$ T, temperature $T = 300$ K, and $N = 10^4$ rubidium atoms.

B. Level structure of Rydberg atoms

Rydberg atoms are highly excited atoms featuring large dipole moments and polarizability. Each eigenstate can be characterized by the quantum numbers n, l, j, m. The energies ϵ_μ depend mainly on the principal quantum number $n \in \{1, 2, 3, \dots\}$ and the angular-momentum quantum number $l = 0, \dots, n-1$ (also denoted by $s, p, d, f, \dots$). The numbers j and m characterize the total angular momentum quantum number and its z projection, respectively. The spectrum of a rubidium atom is depicted in Fig. 2(a), where each column represents a different l. The energy splitting between the highly excited Rydberg states $n \gg 1$ rapidly decreases as n becomes large. In the presence of a static macroscopic magnetic field $\boldsymbol{B} \parallel \boldsymbol{e}_z$, the eigenstates $|\mu\rangle$ are subject to a Zeeman shift, whose linear contribution reads

$$\Delta\epsilon_\mu = \frac{\mu_B|\boldsymbol{B}|}{\hbar}\langle\mu|(\hat{L}_z + g_z\hat{S}_z)|\mu\rangle \equiv K_\mu|\boldsymbol{B}|, \qquad (19)$$

where μ_B is the Bohr magneton, $\hat{L}_z$ is the z projection operator of the angular momentum, $\hat{S}_z$ is the projection of the spin, and g_z is the corresponding gyromagnetic factor. The Zeeman effect can be used to tune specific energy states such that the monochromatic axion field fulfills a resonance condition.

Because the electron is excited so far away from the nucleus, the transition dipole moments of two neighboring Rydberg states with principal quantum numbers $n' = n \pm 1$ are very large and scale as $|\boldsymbol{d}_{\mu,\nu}| \propto n^2$, given that no optical selection rules are violated; cf., Fig. 2(d). Thus, due to their energy spacing and the scaling of their dipole elements, Rydberg atoms are very sensitive to low-frequency and quasistatic electric fields.

C. Sensitivity estimation

Recent experiments using EIT have demonstrated an outstanding sensitivity of Rydberg-atom superhet detectors for sensing electric fields [44]. The superhet configuration consists of two low-energy states $|1\rangle$, $|2\rangle$, and two Rydberg states $|3\rangle$, $|4\rangle$, whose energetic locations are marked in Figs. 2(a) and 2(b). The states $|1\rangle$ and $|2\rangle$ are coupled by the probe laser of frequency ω_p and transition frequency (i.e., Rabi frequency) Ω_p, while the states $|2\rangle$ and $|3\rangle$ are coupled by the coupling laser of frequency $\omega_{\rm C}$ and Rabi frequency $\Omega_{\rm C}$. The Rydberg states are coupled by the axion field of frequency $\omega_{\rm a}$ and Rabi frequency $\Omega_{\rm a} = g_{{\rm a}\gamma\gamma}ca_0|\boldsymbol{d}_{3,4}\cdot\boldsymbol{B}|/\hbar\mathcal{S}$. The corresponding energies ϵ_3 and ϵ_4 are assumed to be close to resonance $\epsilon_4 - \epsilon_3 \approx \hbar\omega_{\rm a}$. The resonance condition can be adjusted using the Zeeman effect [see Fig. 2(c)]. To enhance the signal, the superhet detector uses a local oscillator with frequency $\hbar\omega_{\rm LO} = \epsilon_4 - \epsilon_3$ and Rabi frequency $\Omega_{\rm LO} \gg \Omega_a$ which heterodynes the axion field.

The coupled Rydberg states form the states $|-\rangle$ and $|+\rangle$, which exhibit a slow monochromatic energy splitting $\hbar\Omega(t) = \epsilon_+(t) - \epsilon_-(t) = \hbar\Omega_{\rm LO} + \hbar\Omega_{\rm a}\cos[(\omega_{\rm a} - \omega_{\rm LO})t]$. As $\omega_{\rm a} \approx \omega_{\rm LO}$, we consider $\Omega(t)$ to be quasistatic. Both states are coupled to state $|2\rangle$ with Rabi frequency $\Omega_{\rm C}/\sqrt{2}$. The resulting four-level system is depicted in Fig. 2(d).

The superhet detector senses the axion field via a change of the transmission of the probe laser propagating through a cloud of Rydberg atoms, as sketched in Fig. 2(e). The transmitted intensity as a function of position z is given as $I(z) = I_0\exp[-\alpha(\omega_p)z]$, where $\alpha(\omega_p)$ denotes the linear absorption rate. In the presence of an external electric field, e.g., produced by the axion field, the absorption rate is modified, which can be detected by an intensity change of the transmitted probe laser. The calculation of the absorption rate and the resulting signal-to-noise ratio of the superhet detector is given in detail in Appendix D. As the absorption rate is a property in the nonequilibrium stationary state of the atoms, this measurement can run for arbitrary long times.

The absorption rate for the resonance condition $\hbar\omega_p = \epsilon_2 - \epsilon_1$ is shown in Fig. 2(g) as a function of $\Delta\omega_C = \omega_C - (\epsilon_3 + \epsilon_2)/\hbar$. The absorption rate exhibits a dip around $\Delta\omega_C = 0$ for $\Omega = 0$ (not shown). This is the celebrated EIT affect, which is induced by a destructive interference between the transitions from $|1\rangle$ to $|2\rangle$ and $|3\rangle$ ($|4\rangle$) to $|2\rangle$ in the system's stationary state, preventing the absorption of the probe laser [54,55].

For a finite Ω, the atoms are not perfectly transparent closely around $|\Delta\omega_C| \approx 0$. The energy splitting between the two states $|-\rangle$ and $|+\rangle$ results into two new transparency frequencies at $\Delta\omega_C = \pm\Omega/2$. Their interference shifts the ideal transparency, which would appear for $\Omega = 0$ at $\Delta\omega_C = 0$, and gives rise to high sensitivity of the absorption rate as highlighted in the left inset of Fig. 2(g), which compares the absorption rate for $\Omega = \Omega_{LO}$ and $\Omega = \Omega_{LO} + \Omega_a$. A thorough analysis in Appendix D reveals that the signal-to-noise ratio (SNR) for a total measurement time t_m is given by

$$\mathrm{SNR} = \sqrt{N}\Omega_a\tau, \tag{20}$$

where N is the number of Rydberg atoms, $\tau = \sqrt{T_c t_m}$ is the effective measurement time, and T_c is the effective coherence time,

$$T_c = \frac{4\Omega_p^2\Omega_C^4(1+\Gamma')^2}{\left[\left(\gamma_2 + \frac{\omega_p\sigma}{c}\Gamma\right)\left(\Omega_{LO}^2 + \gamma^2\right) + \Omega_C^2\gamma\right]^3}\frac{\gamma^2\Omega_{LO}^2}{\left(\Omega_{LO}^2 + \gamma^2\right)} \tag{21}$$

with $\gamma = (\gamma_3 + \gamma_4)/2$, where γ_2, γ_3, and γ_4 are the inverse lifetimes of the states $|2\rangle$, $|3\rangle$, and $|4\rangle$, respectively. The Doppler effect for atoms of mass m_R at temperature T is described by the function $\Gamma = \Gamma[\zeta/(\sqrt{2}\sigma)] \geqslant 0$, where $\zeta = \gamma_2 + \gamma\Omega_C^2/(\Omega_{LO}^2 + \gamma^2)$ and $\sigma^2 = k_B T/m_R$, which is given in Eq. (D37). Its derivative $\Gamma' = \partial_x\Gamma(x)\mid_{x\to\zeta/(\sqrt{2}\sigma)}$ is bounded by $-0.5 < \Gamma' < 0$ and has a minor impact on T_c. The Doppler effect thus enhances the dephasing rate $\gamma_2' \to \gamma_2 + \frac{\omega_p\sigma}{c}\Gamma$, which is discussed in detail in Appendix D 7. Equation (20) accounts for the projection noise in the atomic system, which sets the only fundamental limit for the SNR, while photon-shot and measurement noises have been neglected here [48].

As shown in the inset of Fig. 2(g), the SNR exhibits a turnover as a function of the local oscillator strength. For small Ω_{LO}, it increases linearly with Ω_{LO} until it reaches a maximum around $\Omega_{LO} \approx 5\gamma$. For large Ω_{LO}, the SNR vanishes with Ω_{LO}^{-3}. The maximum value of the coherence time is $T_c \approx (\Omega_p/\Omega_C)^2/\gamma$, which determines the optimal SNR.

Using Eqs. (17) and (20), we find an explicit expression for the projected sensitivity of the axion field,

$$g_{a\gamma\gamma,*} = \left(\frac{|K_3 - K_4|}{|\epsilon_3 - \epsilon_4| - m_a c^2}\right)\frac{\hbar}{\tau\sqrt{N}|\boldsymbol{d}_{3,4}|}\sqrt{\frac{\hbar}{2\rho c^5 m_a^2 l_B^4}}, \tag{22}$$

where K_3, K_4 are defined in Eq. (19). The first fraction represents the inverse magnetic field B_{res} required for establishing a resonance condition, which suggests using states featuring similar Zeeman parameters $K_3 \approx K_4$ and a large detuning, as long as the external magnetic field $B_{res} \lessapprox 10$ T is experimentally feasible. In the proposed Rydberg-atom detector, the magnetic field fulfills thus two tasks: (i) it establishes the resonance condition between the Rydberg states, which enhances the sensitivity to the electric field; (ii) it generates the axion-sourced electric field according to Eq. (17). The second fraction in Eq. (22) represents the minimal electric field which can be detected with the superhet configuration.

To estimate the projected sensitivity achievable with Rydberg atoms, we consider the states $|1\rangle = (n = 5, l = 0, j = 1/2, m = 1/2)$, $|2\rangle = (n = 100, l = 1, j = 3/2, m = 1/2)$, $|3\rangle = (n = 100, l = 2, j = 5/2, m = 1/2)$, and $|4\rangle = (n = 99, l = 3, j = 7/2, m = 1/2)$ of rubidium atoms. Their energies and dephasing rates can be calculated using the ARC package [56]. The dipole matrix element of the Rydberg states is $|\boldsymbol{d}_{3,4}| = 6425 e a_0$ (Bohr radius a_0). In the ultralight axion regime, the optimal magnetic field $|\boldsymbol{B}_{res}| \approx 5.6$ T determined by the first fraction in Eq. (22) is almost independent of the axion mass as $m_a c^2 \ll \epsilon_d - \epsilon_c$. The projected minimal electric fields and the related exclusion limits for $g_{a\gamma\gamma}$ for the measurement times $t_m = 1$ s, 1 h, and 1 month have been discussed in Sec. III A.

According to Eq. (22), the sensitivity scales with $N^{-1/2}$ (i.e., the standard quantum limit) and can thus be further improved by increasing the number of atoms. When using $N = 10^6$ instead of $N = 10^4$ atoms, the minimal detectable $g_{a\gamma\gamma}$ could thus reduce by an additional factor of 10. However, when the density of atoms is too high, interaction effects between the atoms must be taken into account, which might lead to a deviation from the standard quantum scaling.

IV. DISCUSSION

In this article, we have discussed the possibility of detecting the galactic axion field by deploying quantum emitters such as atoms and molecules without using an advanced cavity resonator setup. Our proposal thus facilitates the search in the ultralight axion regime, where the required cavity length becomes unreasonably long. Based on a rigorous quantization of the axion-Maxwell equations, we have derived an effective Hamiltonian that microscopically describes dipole transitions in atoms, molecules, and trapped ions driven by the axion-sourced electric field. This presents an exciting opportunity for repurposing existing electric field detectors based on atomic quantum sensors, which promise performance enhancement by means of quantum engineering [57] for axion detection. In this article, we proposed one such method using highly excited Rydberg states, whose large transition dipole elements make them excellent probes of axion-induced dipole transitions. The proposed protocol offers flexibility and has much potential for improvement, such as an optimized choice of the Rydberg states. Also, other protocols for electric field detection, e.g., based on microwave-optical photon conversion featuring an improved sensitivity by two orders of magnitude compared to the superhet detector [58,59], can be investigated for their potential as dark-matter detectors.

We further conjecture that the dipole transitions can also enhance the sensitivity of other axion detectors, such as helioscopes [18] and phonon polaritons [60]. We note that the direct detection scheme proposed here is different from previous protocols using Rydberg atoms, which employ either the atoms for an indirect detection of the axion-sourced photon in a cavity [61], or the coupling of the electron spin to the axion wind [62–64].

As with all axion detectors, the sensitivity and a possible dark-matter signal method can be easily tested: (i) via the expected long-lasting temporal correlation of the axion field; (ii) by checking the response to mock electric signals mimicking the axion-sourced field; (iii) by switching off the magnetic field, for which the axion-sourced signal will disappear. The last criterion can be regarded as a smoking gun for dark-matter detection.

It is useful to consider further sensitivity improvements of our setup. The sensitivity may be improved for longer measurement campaigns over several years, similar to the one performed by the BACON collaboration [65] searching for the time variation of fundamental constants. In this case, one would also have to carefully account for the stochastic fluctuations of the axion dark matter field. Another avenue might be to seek improvements in the measurement process itself to facilitate sensing of weaker electric fields, e.g., by using stronger probe fields. The sensitivity estimate of the superhet detector for weak probe fields shows that the SNR is proportional to Ω_p/Ω_C, i.e., it improves for stronger probe fields. However, this requires the development of nonperturbative theoretical methods, e.g., based on the photon-resolved Floquet theory [66], to accurately predict the spectroscopic signatures of the axion dark matter. One interesting possibility proposed in [67] is to use trapped ion crystals, which can achieve electric field sensitivities of 100 nV m^{-1}. Moreover, trapping the Rydberg atoms in an optical lattice can further help to mitigate the Doppler effect, and would allow for complex quantum operations to mitigate measurement noise [43,68].

ACKNOWLEDGMENTS

This work is supported by the Guangdong Provincial Key Laboratory (Grant No. 2019B121203002), the MURI-ARO Grant No. W911NF17-1-0323 through UC Santa Barbara, the AFOSR Grant No. FA9550-23-1-0598, and the Shanghai Municipal Science and Technology Major Project through the Shanghai Research Center for Quantum Sciences (Grant No. 2019SHZDZX01).

APPENDIX A: QUANTIZATION OF THE AXION-MAXWELL EQUATIONS

Here, we perform a rigorous quantization of the axion-Maxwell equations. The structure of this Appendix is as follows: In Appendix A 1 we introduce the classical axion-Maxwell equations. In Appendix A 2, we show how to accurately quantize these equations by microscopically deriving the corresponding Hamiltonian.

1. Classical axion-Maxwell equations

The relativistic Lagrangian density describing the dynamics of the pseudoscalar axion field a is given by [7]

$$\begin{aligned}\mathcal{L} = &-\frac{1}{4\mu_0}F_{\alpha\beta}F^{\alpha\beta} - A_\alpha J^\alpha \\ &+\frac{1}{2c\hbar}\partial_\alpha a \partial^\alpha a - \frac{1}{2}\frac{m_a^2c^4}{c^3\hbar^3}a^2 - \frac{g_{a\gamma\gamma}}{4\mu_0}aF_{\alpha\beta}\tilde{F}^{\alpha\beta}, \quad \text{(A1)}\end{aligned}$$

where the covariant electromagnetic field tensor $F_{\alpha\nu} = \partial_\alpha A_\beta - \partial_\beta A_\alpha$ can be expressed in terms of the covariant 4-vector potential $A^\alpha = (\phi, \boldsymbol{A})$. The labels $\alpha, \beta, \gamma, \delta \in \{ct, x, y, z\}$ represent space-time coordinates. The covariant electric 4-current is given as $J^\alpha = (c\rho, \boldsymbol{J})$. The dual tensor of the electromagnetic field is defined by $\tilde{F}^{\alpha\beta} = \frac{1}{2}\epsilon^{\alpha\beta\gamma\delta}F_{\gamma\delta}$, where $\epsilon^{\alpha\beta\gamma\delta}$ is the dyadic tensor. The electric and magnetic fields can be obtained via

$$\boldsymbol{E} = -\nabla\phi - \dot{\boldsymbol{A}} \quad \text{and} \quad \boldsymbol{B} = \nabla\times\boldsymbol{A}. \quad \text{(A2)}$$

Using the Euler-Lagrange equations and the Bianchi identity, we find the following relativistic equations of motion for the above-introduced fields:

$$\begin{aligned}\partial_\alpha F^{\alpha\beta} &= J^\beta - g_{a\gamma\gamma}\tilde{F}^{\alpha\beta}\partial_\alpha a, \\ \left(\frac{1}{2c\hbar}\partial_\alpha\partial^\alpha + \frac{m_a^2c^4}{c^3\hbar^3}\right)a &= -\frac{g_{a\gamma\gamma}}{4\mu_0}F_{\alpha\beta}\tilde{F}^{\alpha\beta}, \\ \partial_\alpha\tilde{F}^{\alpha\beta} &= 0, \quad \text{(A3)}\end{aligned}$$

which in terms of the electric, magnetic, and axion fields provide the axion-Maxwell equations given in Eqs. (1)–(5).

2. Quantization

Using the definition of the electromagnetic field operators in Eqs. (10)–(13), we can show that the canonical commutation relations are indeed fulfilled:

$$\begin{aligned}[\hat{a}(\boldsymbol{r}), \hat{\pi}(\boldsymbol{r}')] &= i\hbar^2c^3\delta(\boldsymbol{r}-\boldsymbol{r}'), \\ [\hat{A}_\alpha(\boldsymbol{r}), \hat{B}_\beta(\boldsymbol{r}')] &= 0, \\ [\hat{A}_\alpha(\boldsymbol{r}), \tilde{E}^\perp_{c,\beta}(\boldsymbol{r}')] &= -\frac{\hbar}{\epsilon_0}\cdot\delta^\perp_{\alpha,\beta}(\boldsymbol{r}-\boldsymbol{r}'), \\ [\hat{B}_\alpha(\boldsymbol{r}), \tilde{E}^\perp_{c,\beta}(\boldsymbol{r}')] &= \frac{\hbar}{\epsilon_0}\epsilon_{\alpha,\beta,\gamma}\frac{d}{dx_\gamma}\delta(\boldsymbol{r}-\boldsymbol{r}'), \quad \text{(A4)}\end{aligned}$$

where $\alpha, \beta, \gamma \in \{x, y, z\}$. All other commutation relations vanish. We refer to Ref. [49] for the technical definition of $\delta^\perp_{\alpha,\beta}(\boldsymbol{r})$.

We are now in a position to derive the nonrelativistic axion-Maxwell equations. The electric and magnetic Gaussian equations are fulfilled since

$$\nabla\cdot\hat{\boldsymbol{E}}_c = \nabla\cdot(\hat{\boldsymbol{E}}^\perp_c + \boldsymbol{E}^\parallel_c) = \frac{\hat{\rho}}{\epsilon_0}, \quad \text{(A5)}$$

where we have used that $\nabla\cdot\hat{\boldsymbol{E}}^\perp_c = \boldsymbol{0}$ and $\nabla\cdot\boldsymbol{E}^\parallel_c = \hat{\rho}/\epsilon_0$ because of the parametrization in Eqs. (11) and (12). Using now the relation of the canonical and physical electric fields in Eq. (6), we obtain the electric Gauss equation. For the same reason, we also find $\nabla\cdot\hat{\boldsymbol{B}} = \boldsymbol{0}$, i.e., the magnetic Gauss equation in Eq. (3).

The Faraday and Ampere equations can be constructed by means of the Heisenberg equations of motion,

$$\dot{\hat{O}} = \frac{i}{\hbar}[\hat{H}, \hat{O}]. \tag{A6}$$

The derivation follows essentially the same lines as the common Maxwell equations upon simply replacing $\hat{\boldsymbol{E}}$ by $\hat{\boldsymbol{E}}_c$. Using the commutation relations in Eq. (A4), we obtain

$$\begin{aligned}
\dot{\hat{\boldsymbol{B}}} &= -\nabla \times \hat{\boldsymbol{E}}_c^{\perp} + c g_{a\gamma\gamma} \nabla \times (\hat{a}\hat{\boldsymbol{B}}), \\
\dot{\hat{\boldsymbol{E}}}_c^{\parallel} &= -\frac{1}{\epsilon_0}\boldsymbol{J}^{\parallel}, \\
\dot{\hat{\boldsymbol{E}}}_c^{\perp} &= -\frac{1}{\epsilon_0}\boldsymbol{J}^{\perp} + c^2 \nabla \times \hat{\boldsymbol{B}} \\
&\quad - \nabla \times [c g_{a\gamma\gamma}\hat{a}(\hat{\boldsymbol{E}}_c - c g_{a\gamma\gamma}\hat{a}\hat{\boldsymbol{B}})].
\end{aligned} \tag{A7}$$

In the magnetic equation, we can replace $\hat{\boldsymbol{E}}_c^{\perp} \to \hat{\boldsymbol{E}}_c$ as $\nabla \times \hat{\boldsymbol{E}}_c^{\parallel} = \boldsymbol{0}$ since $\hat{\boldsymbol{E}}_c^{\parallel} = -\nabla\hat{\phi}$ for the electrostatic potential $\hat{\phi}$ defined in Eq. (12). Moreover, the notion and derivation of $\boldsymbol{J}^{\perp}$ and $\boldsymbol{J}^{\parallel}$, which fulfill $\boldsymbol{J} = \boldsymbol{J}^{\parallel} + \boldsymbol{J}^{\perp}$, can be found in standard textbooks on quantum electrodynamics, e.g., [49]. We proceed to combine the longitudinal and transversal electric equations

$$\begin{aligned}
\dot{\hat{\boldsymbol{E}}}_c &= \dot{\hat{\boldsymbol{E}}}_c^{\parallel} + \dot{\hat{\boldsymbol{E}}}_c^{\perp} \\
&= -\frac{\boldsymbol{J}}{\epsilon_0} + c^2\nabla \times \hat{\boldsymbol{B}} - c g_{a\gamma\gamma}\nabla \times (\hat{a}\hat{\boldsymbol{E}}_c) \\
&\quad + c^2 g_{a\gamma\gamma}^2 \hat{a}\nabla \times (\hat{a}\hat{\boldsymbol{B}}) - c^2 g_{a\gamma\gamma}^2 (\hat{a}\hat{\boldsymbol{B}}) \times \nabla\hat{a}.
\end{aligned} \tag{A8}$$

Resolving the magnetic equation in Eq. (A7) for $c g_{a\gamma\gamma}\nabla \times (\hat{a}\hat{\boldsymbol{B}})$ and inserting into the electric equation (A8), we obtain

$$\begin{aligned}
\dot{\hat{\boldsymbol{E}}}_c &= -\frac{\boldsymbol{J}}{\epsilon_0} + c^2\nabla \times \hat{\boldsymbol{B}} - c g_{a\gamma\gamma}\nabla \times (\hat{a}\hat{\boldsymbol{E}}_c) \\
&\quad + c g_{a\gamma\gamma}\hat{a}\dot{\hat{\boldsymbol{B}}} + c g_{a\gamma\gamma}\hat{a}\nabla \times \boldsymbol{E}_c - c^2 g_{a\gamma\gamma}^2(\hat{a}\hat{\boldsymbol{B}}) \times \nabla\hat{a} \\
&= -\frac{\boldsymbol{J}}{\epsilon_0} + c^2\nabla \times \hat{\boldsymbol{B}} + c^2 g_{a\gamma\gamma}\hat{a}\dot{\hat{\boldsymbol{B}}} \\
&\quad + c g(\hat{\boldsymbol{E}}_c - c g_{a\gamma\gamma}\hat{a}\hat{\boldsymbol{B}}) \times \nabla\hat{a}.
\end{aligned} \tag{A9}$$

Using now the relation of the canonical and physical electric field operators in Eq. (6), we readily find the Faraday and Ampere equations in Eqs. (4), (2), and (5), respectively.

We continue to construct the Heisenberg equations of motion for the axion field, which read

$$\dot{a} = \pi, \tag{A10}$$

$$\begin{aligned}
\dot{\pi} &= c^2\nabla^2\hat{a} - \frac{m_a^2 c^4}{\hbar^2}\hat{a} + \hbar c^3\sqrt{\frac{\epsilon_0}{\mu_0}} g_{a\gamma\gamma}\hat{\boldsymbol{E}}_c \cdot \hat{\boldsymbol{B}} \\
&\quad - \hbar c^3\frac{1}{\mu_0} g_{a\gamma\gamma}^2 \hat{a}\hat{\boldsymbol{B}} \cdot \hat{\boldsymbol{B}}.
\end{aligned} \tag{A11}$$

Upon replacing the canonical electric field by the physical one according to Eq. (6), we obtain

$$\dot{\pi} = c^2\nabla^2\hat{a} - \frac{m_a^2 c^4}{\hbar^2}\hat{a} + \hbar c^3\sqrt{\frac{\epsilon_0}{\mu_0}} g_{a\gamma\gamma}\hat{\boldsymbol{E}} \cdot \hat{\boldsymbol{B}}. \tag{A12}$$

Deriving Eq. (A10) with respect to time and inserting Eq. (A12), we readily obtain the axion equation of motion in Eq. (5).

APPENDIX B: MULTIPOLAR HAMILTONIAN

The minimal-coupling Hamiltonian in Eq. (7) is inconvenient to deal with because of the vector potential $\hat{\boldsymbol{A}}$ that appears quadratically. This causes more complicated expressions when calculating, e.g., the spectroscopic response of quantum systems. Moreover, the vector potential $\hat{\boldsymbol{A}}$ is not a physical observable. For this reason, we will bring the Hamiltonian into the so-called multipolar form that contains only the electric and magnetic fields [49]. This is done by means of the Power-Zienau transformation, which we review here shortly [50]. To this end, we restrict our investigation to systems with only bounded charges, such as atoms, molecules, and similar quantum emitters. We will specify atoms in the following for clarity. Accordingly, the summation over η in Eq. (7) will be modified into a double summation over $i \in \{1, \dots, N\}$, labeling atoms, and $j \in \{1, \dots, N_c\}$, labeling the charges associated with a particular atom. The center of mass of atom i will be denoted by $\boldsymbol{R}_i$, while the position of the charges belonging to this atom is denoted by $\boldsymbol{r}_{i,j}$.

The Power-Zienau transformation is defined by the unitary operator

$$\hat{U} = \exp\left[-i\frac{1}{\hbar}\int d\boldsymbol{r}^3 \hat{\boldsymbol{P}}(\boldsymbol{r}) \cdot \hat{\boldsymbol{A}}(\boldsymbol{r})\right], \tag{B1}$$

where

$$\begin{aligned}
\hat{\boldsymbol{P}}(\boldsymbol{r}) &= \sum_{i,j}\hat{\boldsymbol{n}}_{i,j}(\boldsymbol{r}), \\
\hat{\boldsymbol{n}}_{i,j}(\boldsymbol{r}) &= q_{i,j}(\hat{\boldsymbol{r}}_{i,j} - \boldsymbol{R}_i)\int_0^1 du\, \delta[\boldsymbol{r} - \boldsymbol{R}_i - u(\hat{\boldsymbol{r}}_{i,j} - \boldsymbol{R}_i)]
\end{aligned} \tag{B2}$$

denote the macroscopic polarization and the polarization generated by the particles $\eta = (i, j)$ carrying charge $q_{i,j}$, respectively. The Power-Zienau transformation has the following effect on the system operators:

$$\begin{aligned}
\hat{\boldsymbol{r}}'_{i,j} &= \hat{\boldsymbol{r}}_{i,j}, \\
\hat{\boldsymbol{p}}'_{i,j} &= \hat{\boldsymbol{p}}_{i,j} - \frac{q_e}{c}\hat{\boldsymbol{A}}(\hat{\boldsymbol{r}}_{i,j}) - \int d\boldsymbol{r}^3 \hat{\boldsymbol{n}}_{i,j}(\boldsymbol{r}) \times \hat{\boldsymbol{B}}(\boldsymbol{r}), \\
\hat{d}'_{\boldsymbol{k},\lambda} &= \hat{d}_{\boldsymbol{k},\lambda} + \left(\frac{i}{\hbar}\right)\sqrt{\frac{\hbar}{2\epsilon_0\omega_{\boldsymbol{k}}}}\boldsymbol{e}_{\boldsymbol{k},\lambda} \cdot \hat{\boldsymbol{P}}(\boldsymbol{k}).
\end{aligned} \tag{B3}$$

Consequently, the electromagnetic field operators become

$$\begin{aligned}
\hat{\boldsymbol{A}}'(\boldsymbol{r}) &= \hat{\boldsymbol{A}}(\boldsymbol{r}), \\
\hat{\boldsymbol{B}}'(\boldsymbol{r}) &= \hat{\boldsymbol{B}}(\boldsymbol{r}), \\
\hat{\boldsymbol{E}}_c^{\perp\prime}(\boldsymbol{r}) &= \hat{\boldsymbol{E}}_c^{\perp}(\boldsymbol{r}) + \frac{1}{\epsilon_0}\boldsymbol{P}^{\perp} \equiv \frac{1}{\epsilon_0}\hat{\boldsymbol{D}}_c^{\perp}(\boldsymbol{r}), \\
\hat{\boldsymbol{P}}'(\boldsymbol{r}) &= \hat{\boldsymbol{P}}(\boldsymbol{r}).
\end{aligned} \tag{B4}$$

Thus, only the transverse canonical electric field becomes modified and is shifted by the polarization. The transformed canonical electric field is called the canonical displacement field $\hat{\boldsymbol{D}}_{\mathrm{c}}(\boldsymbol{r})$. Importantly, the displacement field is quantized in terms of the new photonic operators $\hat{d}'_{\boldsymbol{k},\lambda}$:

$$\hat{\boldsymbol{D}}_{\mathrm{c}}^{\perp}(\boldsymbol{r}) = i\sum_{\boldsymbol{k},\lambda}\sqrt{\frac{\hbar\omega_{\boldsymbol{k}}\epsilon_0}{2V}}\boldsymbol{e}_{k,\lambda}[\hat{d}'_{\boldsymbol{k},\lambda}e^{i\boldsymbol{k}\cdot\boldsymbol{r}} - \hat{d}'^{\dagger}_{\boldsymbol{k},\lambda}e^{-i\boldsymbol{k}\cdot\boldsymbol{r}}], \quad \text{(B5)}$$

and not the canonical electric field $\hat{\boldsymbol{E}}_{\mathrm{c}}(\boldsymbol{r})$. However, one should keep in mind that the electric field $\hat{\boldsymbol{E}}$ is the actual physical observable. Away from the matter where $\hat{\boldsymbol{P}}(\boldsymbol{r}) = \boldsymbol{0}$, the canonical displacement field is equivalent to the canonical electromagnetic field $\hat{\boldsymbol{D}}_{\mathrm{c}}(\boldsymbol{r}) = \epsilon_0\hat{\boldsymbol{E}}_{\mathrm{c}}(\boldsymbol{r})$. In the absence of free charges, the displacement field is entirely transverse and reads

$$\hat{\boldsymbol{D}}_{\mathrm{c}}^{\perp}(\boldsymbol{r}) = \hat{\boldsymbol{D}}_{\mathrm{c}}(\boldsymbol{r}) = \epsilon_0\hat{\boldsymbol{E}}_{\mathrm{c}}(\boldsymbol{r}) + \hat{\boldsymbol{P}} \quad \text{(B6)}$$

as the longitudinal polarization fulfills $\hat{\boldsymbol{P}}^{\parallel} = \epsilon_0\hat{\boldsymbol{E}}_{\mathrm{c}}^{\parallel} = \boldsymbol{0}$ in the absence of free charges as considered here.

The multipolar Hamiltonian reads

$$\hat{H}_{\mathrm{ALM}} = \hat{H}_{\mathrm{M}} + \hat{H}_{\mathrm{L}} + \hat{H}_{\mathrm{LM}} + \hat{H}_{\mathrm{A}} + \hat{H}_{\mathrm{Int}}, \quad \text{(B7)}$$

where the transformed matter Hamiltonian is given by

$$\hat{H}_{\mathrm{M}} = \sum_{i,j}\frac{\hat{p}_{ij}^2}{2m_{ij}} + \frac{1}{2\epsilon_0}\sum_{i,j,i',j'}\frac{q_{ij}q_{i'j}}{|\hat{\boldsymbol{r}}_{ij} - \hat{\boldsymbol{r}}_{i'j'}|} + \frac{1}{2\epsilon_0}\int d\boldsymbol{r}^3|\hat{\boldsymbol{P}}^{\perp}(\boldsymbol{r})|^2. \quad \text{(B8)}$$

The last term represents the polarization self-energy. The electromagnetic field Hamiltonian is now given as

$$\hat{H}_{\mathrm{L}} = \frac{1}{2}\int d\boldsymbol{r}^3\left[\frac{1}{\epsilon_0}\hat{\boldsymbol{D}}_{\mathrm{c}}^{\perp 2}(\boldsymbol{r}) + \frac{1}{\mu_0}\hat{\boldsymbol{B}}^2(\boldsymbol{r})\right] = \sum_{\boldsymbol{k},x}\hbar\omega_{\boldsymbol{k}}\left(\hat{d}'^{\dagger}_{\boldsymbol{k}\lambda}\hat{d}'_{\boldsymbol{k}\lambda} + \frac{1}{2}\right), \quad \text{(B9)}$$

where in the second equality we have expressed it in terms of the new photonic operators. The transformed light-matter coupling now reads

$$H_{\mathrm{LM}} = -\int d\boldsymbol{r}^3\hat{\boldsymbol{P}}(\boldsymbol{r})\cdot\hat{\boldsymbol{D}}_{\mathrm{c}}^{\perp}(\boldsymbol{r}) - \int d\boldsymbol{r}^3\hat{\boldsymbol{M}}(\boldsymbol{r})\cdot\hat{\boldsymbol{B}}(\boldsymbol{r}) + \sum_{ij}\frac{1}{2m_{ij}c^2}\left\{\int d\boldsymbol{r}^3[\hat{n}_{ij}(\boldsymbol{r})\times\hat{B}(\boldsymbol{r})]\right\}^2. \quad \text{(B10)}$$

The first term describes the coupling of the electric dipole moment to the displacement field. The second term is the coupling of the magnetic dipole moment (thoroughly defined in Ref. [49]) to the magnetic field. The third term describes the coupling of the electric dipole density to the magnetic field. Yet, as it is divided by the rest energy of the charges $m_{ij}c^2$, this term can be safely neglected.

The free axion Hamiltonian

$$\hat{H}_A = \frac{1}{2}\int d\boldsymbol{r}\left[\frac{\hat{\pi}^2}{\hbar c^3} + \frac{1}{c\hbar}\nabla\hat{a}\cdot\nabla\hat{a} + \frac{m_{\mathrm{a}}^2c^4}{c^3\hbar^3}\hat{a}^2\right]$$

remains unchanged, while the transformed axion-light-matter coupling Hamiltonian now reads

$$\hat{H}_{\mathrm{Int}} = \int d\boldsymbol{r}^3\ cg_{\mathrm{a}\gamma\gamma}[\hat{a}(\hat{\boldsymbol{D}}_{\mathrm{c}} - \hat{\boldsymbol{P}})\cdot\hat{\boldsymbol{B}}] + \int d\boldsymbol{r}^3\ \frac{1}{2\mu_0}g_{\mathrm{a}\gamma\gamma}^2\hat{a}^2\hat{\boldsymbol{B}}\cdot\hat{\boldsymbol{B}}, \quad \text{(B11)}$$

where we have used that $c^2 = 1/(\epsilon_0\mu_0)$.

APPENDIX C: DERIVATION OF THE EFFECTIVE HAMILTONIAN

1. Decoupling transformation

To simplify the following analysis, we consider a strong static magnetic field $\boldsymbol{B}$, which is in agreement with our experimental proposal. The total magnetic field thus reads

$$\hat{\boldsymbol{B}} = \boldsymbol{B} + \hat{\boldsymbol{B}}_{\mathrm{f}}, \quad \text{(C1)}$$

where $\hat{\boldsymbol{B}}_f$ denotes the quantum fluctuations of the field. We now carry out the unitary transformation

$$\hat{U} = \exp\left[i\frac{\epsilon_0}{\hbar}\int d\boldsymbol{r}^3cg_{\mathrm{a}\gamma\gamma}\hat{\boldsymbol{A}}\boldsymbol{B}\hat{a}\right], \quad \text{(C2)}$$

which has the following effect on the system operators:

$$\hat{U}\hat{\boldsymbol{D}}_{\mathrm{c}}\hat{U}^{\dagger} = \hat{\boldsymbol{D}}_{\mathrm{c}} - \epsilon_0cg_{\mathrm{a}\gamma\gamma}\boldsymbol{B}\hat{a} \equiv \hat{\boldsymbol{D}},$$
$$\hat{U}\hat{\pi}\hat{U}^{\dagger} = \hat{\pi} - \epsilon_0c^4\hbar g_{\mathrm{a}\gamma\gamma}\hat{\boldsymbol{A}}\boldsymbol{B} \equiv \hat{\pi}_{\mathrm{tr}}. \quad \text{(C3)}$$

Note that these new field operators also fulfill the canonical commutation relations. Yet, the transformed axion momentum $\hat{\pi}_{\mathrm{tr}}$ is not a physical observable because of the appearance of the electromagnetic vector potential. Thus, the transformed Hamiltonian now reads

$$\begin{aligned}\hat{H} =& \sum_{i,j}\frac{\hat{p}_{ij}^2}{2m_{ij}} + \frac{1}{2\epsilon_0}\sum_{i,j,i',j'}\frac{q_{ij}q_{i'j}}{|\hat{\boldsymbol{r}}_{ij} - \hat{\boldsymbol{r}}_{i'j'}|} \\ &+\frac{1}{2\epsilon_0}\int d\boldsymbol{r}^3|\hat{\boldsymbol{P}}^{\perp}|^2 \\ &+\frac{1}{2}\int d\boldsymbol{r}^3\left[\frac{1}{\epsilon_0}\hat{\boldsymbol{D}}^{\perp 2} + \frac{1}{\mu_0}(\boldsymbol{B} + \hat{\boldsymbol{B}}_{\mathrm{f}})^2\right] \\ &-\int d\boldsymbol{r}^3\frac{1}{\epsilon_0}\hat{\boldsymbol{P}}\cdot\hat{\boldsymbol{D}}^{\perp} - \int d\boldsymbol{r}^3\hat{\boldsymbol{M}}\cdot(\boldsymbol{B} + \hat{\boldsymbol{B}}_{\mathrm{f}})^2 \\ &+\sum_{ij}\frac{1}{2m_{ij}c^2}\left[\int d\boldsymbol{r}^3[\hat{n}_{ij}\times\hat{B}]\right]^2 \\ &- cg_{a\gamma\gamma}\int d\boldsymbol{r}^3\ [\hat{a}(\hat{\boldsymbol{D}} - \hat{\boldsymbol{P}})\cdot\hat{\boldsymbol{B}}_{\mathrm{f}}] \\ &+\int d\boldsymbol{r}^3\ \left[\frac{1}{2\mu_0}g_{\mathrm{a}\gamma}^2\hat{a}^2(\boldsymbol{B} + \hat{\boldsymbol{B}}_f)^2\right] \\ &+\frac{1}{2}\int d\boldsymbol{r}\frac{(\hat{\pi}_{\mathrm{tr}} + \epsilon_0c^4\hbar g_{\mathrm{a}\gamma\gamma}\hat{\boldsymbol{A}}\boldsymbol{B})^2}{\hbar c^3}. \\ &+\frac{1}{2}\int d\boldsymbol{r}\left[\frac{1}{c\hbar}\nabla\hat{a}\cdot\nabla\hat{a} + \frac{m_a^2c^4}{c^3\hbar^3}\hat{a}^2\right].\end{aligned} \quad \text{(C4)}$$

In the transformed Hamiltonian, the axion-polarization coupling is mediated only by the fluctuations of the magnetic field

$\hat{\boldsymbol{B}}_f$, which can thus be neglected. As we see in the fourth line, the polarization couples to the displacement field. For this reason, we have to determine its dynamics to predict whether the axion field can induce some physically measurable effect on the polarization. The equations of motion of the displacement field read

$$\begin{aligned}\frac{d}{dt}\hat{\boldsymbol{D}} &= -\epsilon_0 c g_{a\gamma\gamma}\hat{\pi}_{\mathrm{tr}}(t)\boldsymbol{B} + c^2\nabla\times\hat{\boldsymbol{B}}_f + c^2\nabla\times\hat{\boldsymbol{M}}\\ &\quad + O(g_{a\gamma\gamma}\hat{\boldsymbol{B}}_{\mathrm{f}}),\\ \frac{d}{dt}\hat{\boldsymbol{B}}_{\mathrm{f}} &= -\nabla\times\hat{\boldsymbol{D}},\end{aligned} \tag{C5}$$

which are a linearized version of the axion-Maxwell equations in Eqs. (1)–(5). As c^2 is a large number, we have also constructed the equation of motion for the magnetic field fluctuations. For simplicity, we assume that the axion field is in a coherent state, such that its impulse has the following time evolution:

$$\hat{\pi}_{\mathrm{tr}}(t) \approx \hat{\pi}(t) = \dot{a}(t) = a_0\frac{m_{\mathrm{a}}c^2}{\hbar}\sin\left(\frac{m_{\mathrm{a}}c^2}{\hbar}t\right), \tag{C6}$$

i.e., we neglect the term linear in $g_{a\gamma\gamma}$ [which would give only a contribution $\propto g_{a\gamma\gamma}^2$ in Eq. (C5)], and we consider $\hat{\pi}(t)$ as a classical source term.

2. Solution of the axion-Maxwell equations

To solve the axion-Maxwell equations, we derive the first equation in Eq. (C5) with respect to time, and then insert the magnetic field expression of the second equation. Using identities of vector calculus, we readily arrive at the inhomogeneous wave equation

$$\left[c^2\Delta - \frac{d^2}{dt^2}\right]\hat{\boldsymbol{D}}(r) = -\epsilon_0 c g_{a\gamma\gamma}\dot{\hat{\pi}}(t)\boldsymbol{B}(r), \tag{C7}$$

where the axion field acts as a source term. This equation has the well-known solution

$$\hat{\boldsymbol{D}}(\boldsymbol{r},t) = -\frac{1}{4\pi}\int d^3\boldsymbol{r}'\frac{\boldsymbol{f}(\boldsymbol{r}', t-|\boldsymbol{r}-\boldsymbol{r}'|/c)}{|\boldsymbol{r}-\boldsymbol{r}'|}, \tag{C8}$$

which can be derived, e.g., using the Green's function formalism [69]. In our case, the source term explicitly reads

$$\boldsymbol{f}(r,t) = \epsilon_0 c g_{a,\gamma\gamma} m_{\mathrm{a}}^2 a_0 \cos(m_a t)\boldsymbol{B}(r). \tag{C9}$$

Without loss of generality, we consider the position $\boldsymbol{r} = \boldsymbol{0}$ in the following, as we can place the origin of the coordinate system at the position where we want to sense the displacement field. Expanding the magnetic field in terms of spherical harmonics $Y_{n,l}(\theta', \varphi')$,

$$\begin{aligned}\boldsymbol{B}(\boldsymbol{r}') &= \boldsymbol{B}(r',\theta',\varphi')\\ &= \sum_{n,l}\boldsymbol{B}_{m,l}(r')Y_{m,l}(\theta',\varphi'),\end{aligned} \tag{C10}$$

we find the following expansion for the displacement field:

$$\hat{\boldsymbol{D}}(\boldsymbol{0},t) = \sum_{l,m}\hat{\boldsymbol{D}}_{l,m}(\boldsymbol{0},t). \tag{C11}$$

The partial displacement fields can be expressed as

$$\begin{aligned}\hat{\boldsymbol{D}}_{l,m}(0,t) &= -\frac{\epsilon_0 c g_{a,\gamma\gamma}a_0 m_{\mathrm{a}}^2}{4\pi}\int_0^\infty dr'\int d\theta\int d\varphi \boldsymbol{B}_{l,m}(r')Y_{l,m}(\theta',\varphi')\cos\left(m_{\mathrm{a}}(t-r'/c)\right)r'\sin\theta\\ &= -\frac{\epsilon_0 c g_{a,\gamma\gamma}a_0 m_{\mathrm{a}}^2}{4\pi}\mathcal{K}_{m,n}\int_0^\infty dr'\boldsymbol{B}_{l,m}(r')\cos\left(m_{\mathrm{a}}(t-r'/c)\right)r',\end{aligned} \tag{C12}$$

where the angular dependence is described by the coefficients

$$\mathcal{K}_{m,n} = \frac{1}{2\pi}\int d\theta\int d\varphi Y_{m,n}(\theta,\varphi)\sin\theta. \tag{C13}$$

We emphasize that Eqs. (C11) and (C12) comprise an exact solution of the inhomogeneous wave equation in Eq. (C7).

For a practical reason, we want to bring Eq. (C11) into a more compact form. To this end, we assume that all $\boldsymbol{B}_{l,m}(r')$ are parallel to the magnetic field at the origin $\boldsymbol{B}(0)$. In this case, the displacement field can be expressed as

$$\hat{\boldsymbol{D}}(0,t) = \epsilon_0 c g_{a,\gamma\gamma}a_0\cos(\omega_{\mathrm{a}}t + \tilde{\phi})\boldsymbol{B}(0)\mathcal{S}_B(m_{\mathrm{a}}), \tag{C14}$$

where we have introduced

$$\begin{aligned}\mathcal{S}_B(m_{\mathrm{a}}) &= |\mathcal{F}|,\\ \tilde{\phi} &= \arg\mathcal{F},\\ \mathcal{F} &= -\sum_{l,m}\frac{K_{m,n}}{4\pi|\boldsymbol{B}(0)|}\int_0^\infty dr|\boldsymbol{B}_{l,m}(r)|e^{-im_{\mathrm{a}}r/c}r,\end{aligned} \tag{C15}$$

which incorporates the form of the magnetic field. The phase $\tilde{\phi}$ will be neglected in the following. It is interesting to analyze the form factor $\mathcal{F}$ for small masses m_{a}, such that $e^{-im_{\mathrm{a}}r'/c} \approx 1$. Rescaling the argument of the magnetic field $\boldsymbol{B}'(r) = \boldsymbol{B}(r/\alpha)$, we find that $\mathcal{F}' \to \alpha^2\mathcal{F}$. We thus conclude that the suppression factor

$$\mathcal{S}_B(m_{\mathrm{a}}) \equiv \mathcal{S}\left(\frac{m_{\mathrm{a}}c}{\hbar}l_B\right), \tag{C16}$$

where l_B parametrizes the spatial extend of the magnetic field, scales according to $\mathcal{S}(x) \propto x^2$ for small x. The scaling for large x depends on the particular form of the magnetic field.

3. Example

To illustrate the physical implications of the general solution of the wave equation in Eq. (C11) on a concrete example, we consider an exponentially decaying magnetic field,

$$\boldsymbol{B}_{l,m}(r') = \boldsymbol{B}_{l,m;0}e^{-\gamma r'}, \tag{C17}$$

where $\gamma = 1/l_B$ denotes the inverse decay length. Inserting this into Eq. (C12) and evaluating the integral, we obtain

$$\begin{aligned}\hat{\boldsymbol{D}}_{l,m}(0,t) &= -cg_{\mathrm{a},\gamma\gamma}a_0 m_{\mathrm{a}}^2 e^{im_{\mathrm{a}}t}\mathcal{K}_{m,n}\boldsymbol{B}_{l,m;0}\int_0^\infty dr' e^{-\gamma r'}e^{-im_{\mathrm{a}}r'/c}r' \\ &= -cg_{\mathrm{a},\gamma\gamma}a_0 m_{\mathrm{a}}^2 e^{im_{\mathrm{a}}t}\mathcal{K}_{m,n}\boldsymbol{B}_{l,m;0}\int_0^\infty dr' e^{(-\gamma r'-im_{\mathrm{a}}/c)r'}r' \\ &= cg_{\mathrm{a},\gamma\gamma}a_0 m_{\mathrm{a}}^2 e^{im_{\mathrm{a}}t}\mathcal{K}_{m,n}\boldsymbol{B}_{l,m;0}\int_0^\infty dr'\frac{1}{-\gamma-im_{\mathrm{a}}/c}e^{(-\gamma-im_{\mathrm{a}}/c)r'} \\ &= -cg_{\mathrm{a},\gamma\gamma}a_0 m_{\mathrm{a}}^2 e^{im_{\mathrm{a}}t}\mathcal{K}_{m,n}\boldsymbol{B}_{l,m;0}\frac{1}{(-\gamma-im_{\mathrm{a}}/c)^2}.\end{aligned} \tag{C18}$$

The maximum amplitude of this field has the following scaling properties:

$$\hat{\boldsymbol{D}}_{l,m}^{\max} = \epsilon_0 c g_{\mathrm{a},\gamma\gamma}a_0\boldsymbol{B}_{l,m;0}\mathcal{K}_{m,n}\begin{cases} m_{\mathrm{a}}^2 l_B^2, & m_a l_B \ll 1, \\ 1, & m_a l_B \gg 1.\end{cases} \tag{C19}$$

For small axion masses $m_{\mathrm{a}} l_B \ll 1$, this relation shows that the axion-sourced displacement field is strongly suppressed, in agreement with Eq. (C16). In contrast, for $m_{\mathrm{a}} l_B \gg 1$, the axion-sourced displacement field becomes independent of the axion mass and approaches the solution of the translationally invariant system.

4. Effective Hamiltonian

Based on the previous derivations, we introduce here an effective Hamiltonian, which we use to predict the sensitivity of Rydberg atoms. First, we neglect the fluctuations of the electromagnetic fields and the axion field in the Hamiltonian in Eq. (C4). In doing so, the Hamiltonian reduces to

$$\begin{aligned}\hat{H}(t) &= \sum_{i,j}\frac{\hat{p}_{ij}^2}{2m_{ij}} + \frac{1}{2\epsilon_0}\sum_{i,j,i',j'}\frac{q_{ij}q_{i'j}}{|\hat{\boldsymbol{r}}_{ij}-\hat{\boldsymbol{r}}_{i'j'}|} \\ &\quad + \frac{1}{2\epsilon_0}\int d\boldsymbol{r}^3|\hat{\boldsymbol{P}}^\perp(\boldsymbol{r})|^2 - \int d\boldsymbol{r}^3\frac{1}{\epsilon_0}\hat{\boldsymbol{P}}(\boldsymbol{r})\cdot\boldsymbol{D}^\perp(\boldsymbol{r},t) \\ &\quad - \int d\boldsymbol{r}^3\hat{\boldsymbol{M}}(\boldsymbol{r})\cdot\boldsymbol{B}(\boldsymbol{r}).\end{aligned} \tag{C20}$$

The magnetic field is considered to be static. The dynamics of the displacement field $\boldsymbol{D}^\perp(\boldsymbol{r},t)$ is given by Eq. (C14). Thereby, we implicitly assume that all atoms are located close to the origin as compared to the spatial variation of the magnetic field, i.e., $r_j \approx 0$.

Next, we represent the matter Hamiltonian in the energy basis of the atoms, such that it reads

$$\begin{aligned}\hat{H}_0 &= \sum_{i,j}\frac{\hat{p}_{ij}^2}{2m_{ij}} + \frac{1}{2\epsilon_0}\sum_{i,j,i',j'}\frac{q_{ij}q_{i'j}}{|\hat{\boldsymbol{r}}_{ij}-\hat{\boldsymbol{r}}_{i'j'}|} \\ &= \sum_{i=1}^{N}\sum_{\mu,\nu}\epsilon_\mu^{(i)}|i,\mu\rangle\langle i,\mu|,\end{aligned} \tag{C21}$$

where $\epsilon_\mu^{(i)}$ denotes the energies. Likewise, we expand the magnetization operator

$$\hat{\boldsymbol{M}}(\boldsymbol{r}) = \sum_{i=1}^{N}\sum_{\mu}\boldsymbol{m}_\mu^{(i)}|i,\mu\rangle\langle i,\mu|\delta(\boldsymbol{r}-\boldsymbol{r}_i) \tag{C22}$$

and the polarization operator

$$\hat{\boldsymbol{P}}(\boldsymbol{r}) = \sum_{i=1}^{N}\sum_{\mu,\nu}\boldsymbol{d}_{\mu,\nu}^{(i)}|i,\mu\rangle\langle i,\nu|\delta(\boldsymbol{r}-\boldsymbol{r}_i), \tag{C23}$$

where $\delta(\boldsymbol{r})$ is the three-dimensional delta function. Please note that the magnetization is assumed to be diagonal here, such that it describes the common Zeeman shift in atoms. We assume that the atoms are far apart from each other, such that we can neglect the polarization interaction operator, i.e., the third term in Eq. (C20).

After carrying out all these changes, the effective Hamiltonian reads

$$\begin{aligned}\hat{H}_{\mathrm{eff}}(t) &= \sum_{i=1}^{N}\sum_{\mu}\big[\epsilon_\mu - \boldsymbol{m}_\mu^{(i)}\cdot\boldsymbol{B}_0\big]|i,\mu\rangle\langle i,\mu| \\ &\quad - \sum_{i=1}^{N}\boldsymbol{E}_{\mathrm{a}}(t)\cdot\boldsymbol{d}_{\mu,\nu}^{(i)}|i,\mu\rangle\langle i,\nu|,\end{aligned} \tag{C24}$$

where the axion-sourced electric field is given by

$$\boldsymbol{E}_{\mathrm{a}}(t) = g_{\mathrm{a}\gamma\gamma}ca(t)\boldsymbol{B}_0\mathcal{S}\left(\frac{m_{\mathrm{a}}c}{\hbar}l_B\right). \tag{C25}$$

Thereby, we have defined $\boldsymbol{B}_0 = \boldsymbol{B}(\boldsymbol{r}=\boldsymbol{0})$ as the magnetic field at the origin. The suppression factor, which depends on the axion mass m_{a} and the spatial shape of the magnetic field, has been defined in Eq. (C16). The second term in Eq. (C24) is equivalent to Eq. (16) in the article.

APPENDIX D: SENSITIVITY OF ATOMIC SUPERHETERODYNE DETECTORS

In this Appendix, we give a microscopic derivation of the projected signal-to-noise ratio (SNR) given in Eq. (20) in the main text.

1. Hamiltonian

We describe the system as an effective four-level system whose states are denoted by $|1\rangle$, $|2\rangle$, $|3\rangle$, $|4\rangle$. Their energetic positions are shown in the spectrum in Fig. 2. The corresponding Hamiltonian reads

$$\begin{aligned} H(t) = {} & \epsilon_1|1\rangle\langle 1| + \epsilon_2|2\rangle\langle 2| + \epsilon_3|3\rangle\langle 3| + \epsilon_4|4\rangle\langle 4| \\ & + \frac{\hbar}{2}[\Omega_p e^{i\omega_p t}|2\rangle\langle 1| + \text{H.c.}] \\ & + \frac{\hbar}{2}[\Omega_C e^{i\omega_C t}|3\rangle\langle 2| + \text{H.c.}] \\ & + \frac{\hbar}{2}[(\Omega_{\text{LO}} e^{i\omega_{\text{LO}} t} + \Omega_a e^{i\omega_1 t})|4\rangle\langle 3| + \text{H.c.}\,], \end{aligned} \tag{D1}$$

where ϵ_x with $x = 1, 2, 3, 4$ denote the level energies. The parameters in Eq. (D1) have been already introduced in Sec. III C.

In general, $\omega_{\text{a}} \neq \omega_{\text{LO}}$, but if $|\omega_{\text{a}} - \omega_{\text{LO}}|$ is smaller than all other frequencies in the system, the two Rydberg states can be considered to be coupled by an effective field with frequency ω_{LO} and an adiabatically varying Rabi frequency $\Omega(t) = \Omega_{\text{LO}} + \Omega_{\text{a}} e^{i(\omega_{\text{a}} - \omega_{\text{LO}})t}$. To enable analytical calculations, we will consider Ω to be constant and parametrize it as $\Omega = \Omega_{\text{LO}} + \Omega_{\text{a}}$.

To analytically describe the EIT in the four-level system which is subject to dissipation, we describe the dynamics by the Bloch equation,

$$\frac{d}{dt}\rho = -\frac{i}{\hbar}[H(t), \rho] + \gamma_2 D_{|1\rangle\langle 2|}\rho + \gamma_3 D_{|1\rangle\langle 3|} + \gamma_d D_{|1\rangle\langle 4|}\rho, \tag{D2}$$

where the dissipator is defined by

$$D_{\hat{O}}\rho = \hat{O}\rho\hat{O}^\dagger - \frac{1}{2}(\hat{O}^\dagger\hat{O}\rho + \rho\hat{O}^\dagger\hat{O}), \tag{D3}$$

and γ_2, γ_3, and γ_4 denote the inverse lifetimes of states $|2\rangle$, $|3\rangle$, and $|4\rangle$, respectively.

For the ongoing analysis, we assume the resonance condition $\epsilon_4 - \epsilon_3 = \hbar\omega_{\text{a}}$. Such a resonance condition can be fulfilled by adjusting the energies ϵ_3, ϵ_4 using the Zeeman effect. Transforming the subsystem consisting of the states ϵ_3, ϵ_4 into a frame rotating with ω_{a}, and expressing the Hamiltonian using the diagonal basis of this subsystem, it becomes

$$\begin{aligned} H(t) = {} & \sum_{x=1,2,-,+} \epsilon_x|x\rangle\langle x| \\ & + \frac{\hbar}{2}\bigg[\Omega_p e^{i\omega_p t}|2\rangle\langle 1| + \frac{1}{\sqrt{2}}\Omega_C e^{i\omega_C t}|-\rangle\langle 2| \\ & + \frac{1}{\sqrt{2}}\Omega_C e^{i\omega_C t}|+\rangle\langle 2| + \text{H.c.}\bigg], \end{aligned} \tag{D4}$$

where the energies in the diagonalized subspace are given by $\epsilon_- = \epsilon_3 - \hbar\Omega/2$ and $\epsilon_+ = \epsilon_3 + \hbar\Omega/2$. Accordingly, the Bloch equation reads

$$\frac{d}{dt}\rho = -\frac{i}{\hbar}[H(t), \rho] + \gamma_2 D_{|1\rangle\langle 2|}\rho + \gamma D_{|1\rangle\langle -|}\rho + \gamma D_{|1\rangle\langle +|}\rho, \tag{D5}$$

where the dissipation rate γ is given by $\gamma = \frac{1}{2}(\gamma_3 + \gamma_4)$.

2. Signal operator

In the superhet detection scheme, an external electric field is detected by a change of the transmission of the probe laser through the atom cloud. The transmitted intensity follows thereby the Beer's absorption law

$$I(z) = I_0 \exp[-\rho_N \kappa(\omega_p) z], \tag{D6}$$

where ρ_N is the density of atoms and $\kappa(\omega_p)$ is the absorption cross section of the probe laser. The product of density and absorption cross section is denoted as absorption rate $\alpha(\omega_p) = \rho_N\kappa(\omega_p)$. Using standard methods of spectroscopy [49], one can show that the absorption cross section is proportional to the imaginary part of the *susceptibility* $\chi(\omega_p)$:

$$\begin{aligned} \kappa(\omega_p) &= 2\pi \frac{\omega\, \text{Im}\, \chi(\omega_p)}{c\rho_A n(\omega_p)}, \\ n(\omega_p) &= \sqrt{1 + 4\pi\, \text{Re}\, \chi(\omega_p)}, \end{aligned} \tag{D7}$$

where $n(\omega)$ denotes the refractive index. For small densities ρ_N, we can approximate $n(\omega) = 1$. Moreover, for a small product $\rho_N\kappa(\omega_p)z$, we can linearize Eq. (D6) such that

$$I(z) \approx \frac{\omega_p}{c}\text{Im}\, \chi(\omega_p)z, \tag{D8}$$

which shows that the transmitted intensity is proportional to the imaginary part of the susceptibility.

As we show in the next section, the susceptibility is intimately linked to the operator $\hat{\mathcal{X}} = \sum_{i=1}^N \hat{\mathcal{X}}_i$, where i labels the N atoms in the system, and

$$\begin{aligned} \hat{\mathcal{X}}_i &= \int_0^{t_{\text{m}}} dt \hat{\mathcal{P}}_{2,1}^{(i)}(t) e^{i(\omega_p t + \varphi)} + \text{H.c.}, \\ \hat{\mathcal{P}}_{2,1}^{(i)}(t) &\equiv \hat{U}^\dagger(t)(|2\rangle_i\langle 1| + |1\rangle_i\langle 2|)\hat{U}(t), \end{aligned} \tag{D9}$$

where $\hat{U}(t)$ is the time-evolution operator determined by the Hamiltonian in Eq. (D1). The phase φ is a free parameter. The operator $\hat{\mathcal{X}}$ acts nonlocal in time, which is well defined in the Heisenberg picture. As we will show in the following, the expectation value for $\varphi = \pi/2$ and the variance for all φ of $\hat{\mathcal{X}}$ are proportional to the imaginary part of the susceptibility in the linear-response regime, i.e.,

$$\langle\hat{\mathcal{X}}\rangle \propto \langle\hat{\mathcal{X}}^2\rangle \propto \text{Im}\, \chi(\Omega_p), \tag{D10}$$

where the expectation value is defined by $\langle\bullet\rangle = \text{tr}[\bullet\rho_{\text{st}}]$ with the stationary state of the system for $\Omega_p = 0$ given by $\rho_{\text{st}} = |1\rangle\langle 1|$. Due to its close relation to the susceptibility (and thus to the absorption rate), we refer to $\hat{\mathcal{X}}$ as the susceptibility operator in the following. In Appendix D 8, we thus take the operator $\hat{\mathcal{X}}$ as the basis to determine the SNR of the experimental setup. In doing so, we accurately account for the projection noise, which is the only fundamentally limiting noise source in the experiment [47]. Other noises, like photon shot noise or detection noise, are not considered here.

3. Susceptibility

The susceptibility can be expressed in terms of the linear-response function $S(\boldsymbol{r}, t)$, which determines the polarization in response to an external probe electric field $\hat{\boldsymbol{E}}_p(r, t) = \boldsymbol{E}_{p,0}\cos(\boldsymbol{k}\boldsymbol{r} - \omega_p t)$ [49], i.e.,

$$\hat{\boldsymbol{P}}(\boldsymbol{r}) = \epsilon_0 \int d^3\boldsymbol{r} \int_0^t S(\boldsymbol{r} - \boldsymbol{r}', t - t')\hat{\boldsymbol{E}}_p(r', t')dt'. \tag{D11}$$

We assume here that the probe frequency is close to resonance with the transition between $|1\rangle$ and $|2\rangle$ in the Hamiltonian in Eq. (D1). For this reason, it is sufficient to parametrize the polarization operator as

$$\hat{\boldsymbol{P}}(\boldsymbol{r}) = \sum_{i=1}^{N} \boldsymbol{d}_{1,2}^{(i)} \hat{\mathcal{P}}_{2,1}^{(i)} \delta(\boldsymbol{r} - \boldsymbol{r}_i). \tag{D12}$$

Applying standard first-order perturbation theory to the Hamiltonian in Eq. (D1), we find that the linear-response function is given by [49]

$$S(\boldsymbol{r}, t) = -i\rho_N \frac{|\boldsymbol{d}_{1,2}|^2}{\epsilon_0 \hbar} \langle [\hat{\mathcal{P}}_{2,1}(t), \hat{\mathcal{P}}_{2,1}(0)] \rangle_{\Omega_p = 0}\, \delta(\boldsymbol{r}), \tag{D13}$$

where ρ_N denotes the atom density. Here, we have assumed that all atoms are equal, such that we can neglect the superscript i. The time-evolution is thereby determined for $\Omega_p = 0$. The linear susceptibility can be obtained from the linear-response function via Fourier transformation

$$\begin{aligned}
\chi(\omega_p) &= \int d^3\boldsymbol{r} \int_0^\infty S(r, t) e^{i\omega_p t} dt \\
&= (-i)\rho_N \frac{|\boldsymbol{d}_{1,2}|^2}{\epsilon_0 \hbar} [C(\omega_p) - C(-\omega)^*] \\
&\approx (-i)\rho_N \frac{|\boldsymbol{d}_{1,2}|^2}{\epsilon_0 \hbar} C(\omega_p).
\end{aligned} \tag{D14}$$

For later purpose, we have introduced the correlation function

$$\begin{aligned}
C(t, t') &= \langle \hat{\mathcal{P}}_{1,2}(t) \hat{\mathcal{P}}_{1,2}(t') \rangle|_{\Omega_p=0} \\
&= \langle \hat{\mathcal{P}}_{1,2}(t - t') \hat{\mathcal{P}}_{1,2}(0) \rangle|_{\Omega_p=0} \\
&= C(t - t').
\end{aligned} \tag{D15}$$

Its Fourier transformation is defined via

$$C(\omega) = \int_0^\infty C(t) e^{i\omega t} dt. \tag{D16}$$

In the approximation in Eq. (D14) we have deployed the Kubo-Martin-Schwinger relation $C(\omega) = C(-\omega)e^{\beta\hbar\omega}$ assuming room temperature $1/\beta \approx 25$ meV and probe frequency $\hbar\omega_p > 1$ eV.

4. Calculation of the signal

We calculate the expectation value of the operator $\hat{\mathcal{X}}_i$ in Eq. (D9) in the presence of the probe field $\hat{\boldsymbol{E}}_p(\boldsymbol{r}, t) = \boldsymbol{E}_{p,0} \cos(\boldsymbol{kr} - \omega_p t)$ in first-order perturbation theory in $\Omega_p = |\boldsymbol{d}_{1,2} \cdot \boldsymbol{E}_{p,0}|/\hbar$. As trivially $\langle \hat{\mathcal{X}}_i \rangle_{\Omega_p=0} = 0$, we find

$$\begin{aligned}
\langle \hat{\mathcal{X}}_i \rangle \approx \Omega_p \int_0^{t_\mathrm{m}} dt \int_0^t dt' (-i)[C(t, t') - C(t', t)] \\
\times \cos(\omega_p t') \cos(\omega_p t + \varphi).
\end{aligned} \tag{D17}$$

In agreement with the RWA in the Hamiltonian in Eq. (D1), we neglect the fast oscillating terms $e^{\pm 2\omega_p t}$. In doing so, we find

$$\begin{aligned}
\langle \mathcal{X}_i \rangle &\to \Omega_p \int_0^{t_\mathrm{m}} dt \int_0^t dt' (-i)[C(t, t') - C(t', t)] \\
&\quad \times \left[e^{i(\omega_p t' - \omega_p t + \varphi)} + e^{-i(\omega_p t' - \omega_p t + \varphi)}\right] \\
&= \Omega_p \int_0^{t_\mathrm{m}} dt \int_0^t dt' (-i)[C(t') - C(-t')] \\
&\quad \times [e^{i(-\omega_p t' + \varphi)} + e^{-i(-\omega_p t' + \varphi)}] \\
&\approx \Omega_p \int_0^{t_\mathrm{m}} dt \int_0^\infty dt' (-i)[C(t') - C(-t')] \\
&\quad \times [e^{i(-\omega_p t' + \varphi)} + e^{-i(-\omega_p t' + \varphi)}] \\
&= \Omega_p \int_0^{t_\mathrm{m}} dt (-i)[C(\omega_p) e^{i\varphi} - C(-\omega_p)^* e^{-i\varphi} + \text{H.c.}] \\
&= \Omega_p t_\mathrm{m} (-i)[C(\omega_p) e^{i\varphi} - C(-\omega_p)^* e^{-i\varphi} + \text{H.c.}].
\end{aligned} \tag{D18}$$

Setting $\varphi = \pi/2$ and comparing with Eq. (D14), we obtain

$$\operatorname{Im} \chi(\omega_p) = \frac{1}{2\Omega_p t_\mathrm{m}} \frac{\rho_N |\boldsymbol{d}_{1,2}|^2}{\epsilon_0 \hbar} \langle \hat{\mathcal{X}} \rangle, \tag{D19}$$

which establishes the desired relation between the operator $\hat{\mathcal{X}}$ and the susceptibility.

5. Calculation of the noise

In the same manner, we evaluate the variance of the observable $\hat{\mathcal{X}}$. As Ω_p is assumed to be small, it has a minor influence on the result, and we can set $\Omega_p = 0$. Explicitly, the variance can be evaluated to be

$$\begin{aligned}
\langle \hat{\mathcal{X}}_i \hat{\mathcal{X}}_i \rangle &= \int_0^{t_\mathrm{m}} dt \int_0^{t_\mathrm{m}} dt' \langle \hat{\mathcal{X}}_{1,2}(t) \hat{\mathcal{X}}_{b,a}(t') \rangle_{\Omega_p=0} \\
&\quad \times \cos(\omega_p t' + \varphi) \cos(\omega_p t + \varphi) \\
&\to \frac{1}{2} \int_0^{t_\mathrm{m}} dt \int_0^{t_\mathrm{m}} dt' C(t, t') e^{i(\omega_p t' - \omega_p t)} \\
&= \frac{1}{2} \int_0^{t_\mathrm{m}} dt \int_0^{t_\mathrm{m}} dt' C(t - t') e^{i(\omega_p t' - \omega_p t)} \\
&= \frac{1}{2} \int_0^{t_\mathrm{m}} dt \int_0^t dt' C(t - t') e^{-i(\omega_p t' - \omega_p t)} \\
&\quad + \int_0^{t_\mathrm{m}} dt \int_t^{t_\mathrm{m}} dt' C(t' - t)^* e^{-i(\Omega_p t' - \omega_p t)} \\
&= \frac{1}{2} \int_0^{t_\mathrm{m}} dt \int_0^t dt' C(t') e^{i\omega_p t'} \\
&\quad + \int_0^{t_\mathrm{m}} dt \left[\int_0^{t_\mathrm{m} - t} dt' C(t') e^{i\omega_p t'}\right]^* \\
&= \frac{1}{2} \int_0^{t_\mathrm{m}} dt \int_0^\infty dt' C(t') e^{i\omega_p t'} \\
&\quad + \int_0^{t_\mathrm{m}} dt \left[\int_0^\infty dt' C(t') e^{i\omega_p t'}\right]^* \\
&= \frac{1}{2} t_\mathrm{m} [C(\omega_p) + C(\omega_p)^*].
\end{aligned} \tag{D20}$$

Comparing this result with Eq. (D14), we infer that

$$\operatorname{Im} \chi(\omega_p) = \frac{1}{t_\mathrm{m}} \frac{\rho_N |\boldsymbol{d}_{1,2}|^2}{\epsilon_0 \hbar} \langle \hat{\mathcal{X}}^2 \rangle, \tag{D21}$$

where we have again deployed the Kubo-Martin-Schwinger relation.

6. Electromagnetically induced transparency in a four-level system

In Appendixes D 4 and D 5, we have derived formal expressions for the signal and the noise in terms of the susceptibility. It remains to express the susceptibility in terms of the microscopic system parameters. We achieve this by solving the Bloch equation in Eq. (D2) and finding an explicit expression for the matrix element $\rho_{12}(t)$. To connect this to the susceptibility, we use the relation in first-order perturbation theory,

$$\begin{aligned}\rho_{12}(t) &= \int_0^t (-i)\langle[|1\rangle\langle 2|(t), |2\rangle\langle 1|(t')]\rangle_{\Omega_p=0}\Omega_p e^{i\omega_p t'}\\ &= \int_0^t \tilde{C}(t-t')\Omega_p e^{i\omega_p t'},\end{aligned} \tag{D22}$$

where we have introduced the correlation function $\tilde{C}(t)$ for a notation reason. Performing a (normalized) Fourier transformation, we find

$$\begin{aligned}\overline{\rho}_{21}(\omega_p) &= \lim_{\tau\to\infty}\frac{1}{2\tau}\int_{-\tau}^{\tau}\rho_{12}(t)e^{-i\omega_p t}dt\\ &= \Omega_p\tilde{C}(\omega_p),\end{aligned} \tag{D23}$$

where normalization with 2τ is necessary to avoid a divergence. We note that due to the Kubo-Martin-Schwinger relation and within the RWA, $\tilde{C}(\omega_p) \approx C(\omega_p)$. We thus obtain $C(\omega_p)$ and consequently the susceptibility in Eq. (D14) via

$$C(\omega_p) = \frac{d}{d\Omega_p}\overline{\rho}_{21}(\omega_p)\bigg|_{\Omega_p=0}. \tag{D24}$$

To find an expression for $\overline{\rho}_{21}$, we generalize the standard treatment of the EIT in three-level systems (see, e.g., the textbook by Scully [54]) to the four-level system in Eq. (D1). To start with, we transform the Hamiltonian into a frame rotating with frequencies ω_p and ω_C, such that the resulting time-independent Hamiltonian reads

$$\begin{aligned}H &= \epsilon_{1,\Delta}|1\rangle\langle 1| + \epsilon_{2,\Delta}|2\rangle\langle 2| + \epsilon_{-,\Delta}|-\rangle\langle c_1| + \epsilon_{+,\Delta}|+\rangle\langle +|\\ &\quad+\hbar\frac{\Omega_p}{2}[|2\rangle\langle 1| + |1\rangle\langle 2|] + \hbar\frac{\Omega_C}{2\sqrt{2}}[|-\rangle\langle 2| + |b\rangle\langle -|]\\ &\quad+\hbar\frac{\Omega_C}{2\sqrt{2}}[|+\rangle\langle 2| + |2\rangle\langle +|],\end{aligned} \tag{D25}$$

where the detuned energies are defined by $\epsilon_{1,\Delta} = \epsilon_1$, $\epsilon_{2,\Delta} = \epsilon_2 - \hbar\omega_p$, $\epsilon_{-,\Delta} = \epsilon_- - \hbar\omega_p - \hbar\omega_C$, and $\epsilon_{+,\Delta} = \epsilon_+ - \hbar\omega_p - \hbar\omega_C$. The dissipation terms in the Bloch equation in Eq. (D5) remain unchanged. Explicitly, the Bloch equations for the density matrix $\tilde{\rho}$ in the rotating frame read

$$\begin{aligned}
\frac{d}{dt}\tilde{\rho}_{11} &= \gamma_b\tilde{\rho}_{22} + \gamma\tilde{\rho}_{--} + \gamma\tilde{\rho}_{++} - i\frac{\Omega_p}{2}\tilde{\rho}_{21} + i\frac{\Omega_p}{2}\tilde{\rho}_{12},\\
\frac{d}{dt}\tilde{\rho}_{12} &= -\frac{\gamma_b}{2}\tilde{\rho}_{12} - \frac{i}{\hbar}(\epsilon_{1,\Delta} - \epsilon_{2,\Delta})\tilde{\rho}_{12} - i\frac{\Omega_p}{2}\tilde{\rho}_{22} + i\frac{\Omega_p}{2}\tilde{\rho}_{11} + i\frac{\Omega_C}{\sqrt{8}}\tilde{\rho}_{1-} + i\frac{\Omega_C}{\sqrt{8}}\tilde{\rho}_{1+},\\
\frac{d}{dt}\tilde{\rho}_{1-} &= -\frac{\gamma}{2}\tilde{\rho}_{1-} - \frac{i}{\hbar}(\epsilon_{1,\Delta} - \epsilon_{-,\Delta})\tilde{\rho}_{1-} - i\frac{\Omega_p}{2}\tilde{\rho}_{2-} + i\frac{\Omega_C}{\sqrt{8}}\tilde{\rho}_{12},\\
\frac{d}{dt}\tilde{\rho}_{1+} &= -\frac{\gamma}{2}\tilde{\rho}_{1+} - \frac{i}{\hbar}(\epsilon_{1,\Delta} - \epsilon_{+,\Delta})\tilde{\rho}_{1+} - i\frac{\Omega_p}{2}\tilde{\rho}_{2+} + i\frac{\Omega_C}{\sqrt{8}}\tilde{\rho}_{12},\\
\frac{d}{dt}\tilde{\rho}_{22} &= -\gamma_2\tilde{\rho}_{22} - i\frac{\Omega_p}{2}\tilde{\rho}_{12} + i\frac{\Omega_p}{2}\tilde{\rho}_{21} - i\frac{\Omega_C}{\sqrt{8}}\tilde{\rho}_{-2} + i\frac{\Omega_C}{\sqrt{8}}\tilde{\rho}_{2-} - i\frac{\Omega_C}{\sqrt{8}}\tilde{\rho}_{+2} + i\frac{\Omega_C}{\sqrt{8}}\tilde{\rho}_{2+},\\
\frac{d}{dt}\tilde{\rho}_{2-} &= -\frac{1}{2}(\gamma_2+\gamma)\tilde{\rho}_{2-} - \frac{i}{\hbar}(\epsilon_{2,\Delta} - \epsilon_{-,\Delta})\tilde{\rho}_{2-} - i\frac{\Omega_C}{\sqrt{8}}\tilde{\rho}_{--} - i\frac{\Omega_C}{\sqrt{8}}\tilde{\rho}_{+-} + i\frac{\Omega_C}{\sqrt{8}}\tilde{\rho}_{22} - i\frac{\Omega_p}{2}\tilde{\rho}_{1-},\\
\frac{d}{dt}\tilde{\rho}_{2+} &= -\frac{1}{2}(\gamma_2+\gamma)\tilde{\rho}_{2+} - \frac{i}{\hbar}(\epsilon_{2,\Delta} - \epsilon_{-,\Delta})\tilde{\rho}_{2+} - i\frac{\Omega_C}{\sqrt{8}}\tilde{\rho}_{++} - i\frac{\Omega_C}{\sqrt{8}}\tilde{\rho}_{-+} + i\frac{\Omega_C}{\sqrt{8}}\tilde{\rho}_{22} - i\frac{\Omega_p}{2}\tilde{\rho}_{1+},\\
\frac{d}{dt}\tilde{\rho}_{--} &= -\gamma\tilde{\rho}_{--} - i\frac{\Omega_C}{\sqrt{8}}\tilde{\rho}_{2-} + i\frac{\Omega_C}{\sqrt{8}}\tilde{\rho}_{-2},\\
\frac{d}{dt}\tilde{\rho}_{-+} &= -\gamma\tilde{\rho}_{-+} - \frac{i}{\hbar}(\epsilon_{2,\Delta} - \epsilon_{-,\Delta})\tilde{\rho}_{-+} - i\frac{\Omega_C}{\sqrt{8}}\tilde{\rho}_{2+} + i\frac{\Omega_C}{\sqrt{8}}\tilde{\rho}_{-2},\\
\frac{d}{dt}\tilde{\rho}_{++} &= -\gamma\tilde{\rho}_{++} - i\frac{\Omega_C}{\sqrt{8}}\tilde{\rho}_{2+} + i\frac{\Omega_C}{\sqrt{8}}\tilde{\rho}_{+2}.
\end{aligned} \tag{D26}$$

We aim to find an expression for $\tilde{\rho}_{12}$ in the leading order of Ω_p. As inspection of the Bloch equations reveals that $\tilde{\rho}_{11} \approx 1 \gg \tilde{\rho}_{22}, \tilde{\rho}_{2-}, \tilde{\rho}_{-2}, \tilde{\rho}_{--}, \tilde{\rho}_{2+}, \tilde{\rho}_{-+}, \tilde{\rho}_{++} \propto \Omega_p^2$, we neglect corresponding terms. The three remaining equations are thus

$$\begin{aligned} z\check{\rho}_{12} &= -i\tilde{\epsilon}_{12}\check{\rho}_{12} - i\frac{\Omega_p}{2}\check{\rho}_{22} + i\frac{\Omega_C}{\sqrt{8}}\check{\rho}_{1-} + i\frac{\Omega_C}{\sqrt{8}}\check{\rho}_{1+} + i\frac{\Omega_p}{2}\check{\rho}_{11}, \\ z\check{\rho}_{1-} &= -i\tilde{\epsilon}_{1-}\check{\rho}_{12} - i\frac{\Omega_p}{2}\check{\rho}_{2-} + i\frac{\Omega_C}{\sqrt{8}}\rho_{12}, \\ z\check{\rho}_{1+} &= -i\tilde{\epsilon}_{1+}\check{\rho}_{12} - i\frac{\Omega_p}{2}\check{\rho}_{2+} + i\frac{\Omega_C}{\sqrt{8}}\check{\rho}_{12}, \end{aligned} \tag{D27}$$

which we have already transformed into Laplace space under the assumption that $\rho_{12}(0) = \rho_{1-}(0) = \rho_{1+}(0) = 0$. Operators in Laplace space are marked by an inverted hat, i.e., $\check{\bullet}$. Moreover, we have defined

$$\begin{aligned} \tilde{\epsilon}_{12} &= \frac{1}{\hbar}(\epsilon_1 - \epsilon_2) - \omega_p + i\frac{\gamma_2}{2}, \\ \tilde{\epsilon}_{1-} &= \frac{1}{\hbar}(\epsilon_1 - \epsilon_-) + \omega_p + \omega_C + i\frac{\gamma}{2}, \\ \tilde{\epsilon}_{1+} &= \frac{1}{\hbar}(\epsilon_1 - \epsilon_+) + \omega_p + \omega_C + i\frac{\gamma}{2} \end{aligned} \tag{D28}$$

for a notation reason. Resolving Eq. (D27) for $\check{\rho}_{12}$, we obtain

$$\check{\rho}_{12} = \frac{i\Omega_p\check{\rho}_{11}}{z + i\tilde{\epsilon}_{ab} + \frac{1}{8}\frac{\Omega_C^2}{z+i\tilde{\epsilon}_{1-}} + \frac{1}{8}\frac{\Omega_C^2}{z+i\tilde{\epsilon}_{1+}}}. \tag{D29}$$

We are interested in the long-time behavior of $\tilde{\rho}_{12}(t \to \infty)$. Using $\rho_{11}(t) \approx \rho_{11}(0) = 1$, which in Laplace space becomes $\check{\rho}_{11} = \rho_{11}(0)/z$, we find

$$\begin{aligned} \tilde{\rho}_{12}(t \to \infty) &= \lim_{z\to 0} z\check{\rho}_{12}(z) = \frac{-\Omega_p}{\tilde{\epsilon}_{12} - \frac{1}{8}\frac{\Omega_C^2}{\tilde{\epsilon}_{1-}} - \frac{1}{8}\frac{\Omega_C^2}{\tilde{\epsilon}_{1+}}} \\ &= \overline{\rho}_{12}(\omega_p). \end{aligned} \tag{D30}$$

To establish the second equality, we have transformed the density matrix into the laboratory frame via $\rho_{12}(t \to \infty) = \tilde{\rho}_{12}(t \to \infty)e^{i\omega_p t}$, and we carried out the scaled Fourier transformation in Eq. (D23).

7. Temperature dependence

Usually, the superhet detector is operated at a finite temperature (e.g., $T = 300$ K), which will deteriorate its sensitivity. Two effects have to be taken into account. First, the dephasing rates of the excited states γ_2, γ_3, and γ_4 will increase. The temperature-dependent dephasing rates can be calculated using the Alkali-Rydberg-Calculator (ARC) package [56]. Overall, this effect is relatively small. Secondly, the temperature-induced motion of the atoms will give rise to a Doppler shift concerning the probe and coupling beams. To mitigate this effect, the probe and coupling beams shall propagate in opposing directions, as sketched in Fig. 2(f) in the article. Consequently, both laser frequencies are Doppler-shifted as

$$\begin{aligned} \omega_p &\to \omega_p - \frac{2\pi}{\lambda_p}v, \\ \omega_C &\to \omega_C + \frac{2\pi}{\lambda_C}v, \end{aligned} \tag{D31}$$

where $\lambda_p = 2\pi c/\omega_p$ ($\lambda_C = 2\pi c/\omega_C$) is the wavelength of the probe (coupling) beam, and v is the velocity of an atom parallel to the beams.

The Doppler-averaged density matrix elements can be obtained by evaluating the integral

$$\begin{aligned} &\overline{\rho}_{12D}(\omega_p) \\ &= \int_{-\infty}^{\infty} \tilde{\rho}_{12}\left(\omega_p - \frac{2\pi}{\lambda_p}v, \omega_C + \frac{2\pi}{\lambda_C}v\right)\frac{e^{-\frac{m_R v^2}{2k_B T}}}{\sqrt{2\pi k_B T/m_R}}dv \\ &= \int_{-\infty}^{\infty} \frac{-\Omega_p}{\tilde{\epsilon}_{12} - \frac{2\pi}{\lambda_p}v - \frac{1}{8}\frac{\Omega_C^2}{\tilde{\epsilon}_{1-}} - \frac{1}{8}\frac{\Omega_C^2}{\tilde{\epsilon}_{1+}}}\frac{e^{-\frac{m_R v^2}{2k_B T}}}{\sqrt{2\pi k_B T/m_R}}dv \\ &= \int_{-\infty}^{\infty} \frac{c_1}{c_2 - v}\frac{1}{\sqrt{2\pi}\sigma}e^{-\frac{v^2}{2\sigma^2}}dv, \end{aligned} \tag{D32}$$

where m_R denotes the mass of the Rydberg atoms, and T is the temperature of the thermal cloud. For notation purposes, we have introduced the parameters

$$\begin{aligned} c_1 &= -\frac{\Omega_p\lambda_p}{2\pi}, \\ c_2 &= \frac{\lambda_p}{2\pi}\left(\tilde{\epsilon}_{12} - \frac{1}{8}\frac{\Omega_C^2}{\tilde{\epsilon}_{1-}} - \frac{1}{8}\frac{\Omega_C^2}{\tilde{\epsilon}_{1+}}\right), \\ \sigma &= \sqrt{\frac{k_B T}{m_R}}. \end{aligned} \tag{D33}$$

This integral can be solved analytically. Using that $\mathrm{Im}\, c_2 > 0$, we can transform

$$\begin{aligned} \overline{\rho}_{12D}(\omega_p) &= \int_{-\infty}^{\infty} dv \int_0^{\infty} dx(-i)\frac{c_1}{\sqrt{2\pi}\sigma}e^{i(c_2-v)x}e^{-\frac{v^2}{2\sigma^2}} \\ &= (-i)\frac{c_1}{\sqrt{2\pi}\sigma}\sqrt{2\pi}\sigma\int_0^{\infty} dx e^{-\frac{\sigma^2}{2}x^2 + ic_2x} \\ &= (-i)\frac{c_1}{\sqrt{2\pi}\sigma}\sqrt{2\pi}\sigma e^{-\frac{c_2^2}{2\sigma^2}}\int_0^{\infty} dx e^{-\frac{\sigma^2}{2}(x - i\frac{c_2}{\sigma^2})^2} \\ &= (-i)\frac{c_1}{\sqrt{2\pi}\sigma}\sqrt{2\pi}\sigma e^{-\frac{c_2^2}{2\sigma^2}}\int_{-i\frac{c_2}{\sigma^2}}^{\infty} dx e^{-\frac{\sigma^2}{2}x^2} \\ &= (-i)\frac{c_1}{\sqrt{2\pi}\sigma}\sqrt{2\pi}\sigma e^{-\frac{c_2^2}{2\sigma^2}}\frac{\sqrt{2}}{\sigma}\int_{-i\frac{c_2}{\sqrt{2}\sigma}}^{\infty} dx e^{-x^2} \\ &= (-i)c_1\frac{\sqrt{2}}{\sigma}e^{-\frac{c_2^2}{2\sigma^2}}\frac{\sqrt{\pi}}{2}\left[1 - \mathrm{erf}\left(-i\frac{c_2}{\sqrt{2}\sigma}\right)\right], \end{aligned} \tag{D34}$$

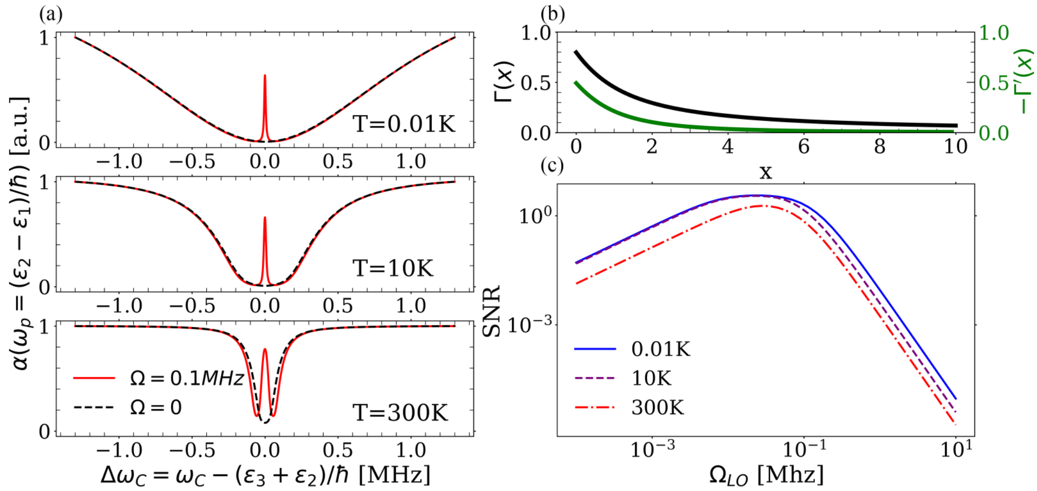

FIG. 3. (a) Absorption rate as a function of $\Delta\omega_\mathrm{C}$ for three different temperatures. (b) Doppler-effect form function $\Gamma(x)$ and its derivative $\Gamma'(x)$. (c) SNR as a function of local oscillator strength for three different temperatures. Parameters are $\Omega_p = 1.7$ MHz, $\Omega_\mathrm{C} = 23$ MHz, and $B_\mathrm{res} = 5.6$ T. If not specified differently, the parameters are the same as in Fig. 2(g).

where in the last step we have introduced the complex-valued error function $\mathrm{erf}(z)$. We continue to bring this into a form that can be more conveniently analyzed. To this end, we expand the error function as a continued fraction,

$$\mathrm{erf}(z) = 1 - \frac{1}{\sqrt{\pi}} \frac{e^{-z^2}}{z + \frac{1}{2z + \frac{2}{z + \frac{3}{z + \cdots}}}}, \tag{D35}$$

such that we can express the density-matrix element as

$$\tilde{\rho}_{12D}(\omega_p) = \frac{c_1}{c_2 + i\sigma\Gamma[-ic_2/(\sqrt{2}\sigma)]}, \tag{D36}$$

where we have defined the form function

$$\Gamma(z) = \frac{\sqrt{2}}{2z + \frac{2}{z + \frac{3}{z + \cdots}}} = \frac{\sqrt{2}}{\sqrt{\pi}} \frac{e^{-z^2}}{1 - \mathrm{erf}(z)} - \sqrt{2}z. \tag{D37}$$

As this function describes the impact of the Doppler effect on the susceptibility, we will refer to it as the Doppler-effect form function in the following.

Putting everything together, the imaginary part of the susceptibility is given by

$$\mathrm{Im}\,\chi(\omega_p) = \frac{\rho_N |\boldsymbol{d}_{1,2}|^2}{\epsilon_0 \hbar} \mathrm{Im}\, \frac{c_1}{c_2 + i\sigma\Gamma[-ic_2/(\sqrt{2}\sigma)]}, \tag{D38}$$

which is proportional to the absorption rate $\alpha(\omega_p)$. We emphasize that this expression is nonperturbative for all parameters. Inspection of Eq. (D38) shows that the Doppler effect enhances the dephasing rate $\gamma_2' \rightarrow \gamma_2 + \frac{\omega_p \sigma}{c}\Gamma[-ic_2/(\sqrt{2}\sigma)]$. We depict the absorption rate as a function of coupling laser frequency detuning $\Delta\omega_\mathrm{C} = \omega_\mathrm{C} - (\epsilon_3 - \epsilon_2)/\hbar$ for different temperatures in Fig. 3(a).

Without local oscillator $\Omega_\mathrm{LO} = 0$, the absorption rate exhibits a broad single dip at $\Delta\omega_\mathrm{C} = 0$, which is the celebrated EIT. Since $\mathrm{Im}\,\chi(\omega_p) \propto \gamma$, the EIT is not complete for $T = 300$ K, as γ increases for increasing temperature. The width of the dip scales with $\propto 1/\gamma_2'$ and thus decreases for larger temperatures.

For a finite local oscillator strength $\Omega = 0.1$ MHz, the two levels $|3\rangle$ and $|4\rangle$ mix, which leads to constructive interference at $\Delta\omega_\mathrm{C} = 0$ and destroys the EIT. This generates a peak in the absorption rate, whose width is proportional to γ. The height of the peak sensitively depends on Ω.

8. Signal-to-noise ratio

As the susceptibility sensitively depends on Ω at the resonance condition $\Delta\omega_\mathrm{C} = 0$, the superhet detector operates under these circumstances, in which

$$c_2 = i\frac{\lambda_p}{2\pi}\left(\gamma_2 + \frac{\Omega_\mathrm{C}^2 \gamma}{\Omega^2 + \gamma^2}\right). \tag{D39}$$

Based on Eqs. (D19), (D21), and (D38), we can now evaluate the SNR for the operator $\hat{\mathcal{X}}$. Recalling that the total Rabi coupling between the Rydberg states consists of the local oscillator and the axion-induced dipole transitions $\Omega = \Omega_\mathrm{LO} + \Omega_\mathrm{a}$, we find that the signal for small Ω_a is given by

$$\begin{aligned} \delta\langle\hat{\mathcal{X}}\rangle &= \Omega_\mathrm{a} \frac{d}{d\Omega_\mathrm{a}} \langle\hat{\mathcal{X}}\rangle|_{\Omega_a = 0} \\ &= \frac{2(1+\Gamma')}{\left(\gamma_2 + \frac{\omega_p\sigma}{c}\Gamma + \frac{\Omega_\mathrm{C}^2\gamma}{\Omega_\mathrm{LO}^2 + \gamma^2}\right)^2} \frac{\Omega_\mathrm{C}^2 \gamma 2\Omega_\mathrm{LO} N \Omega_p \Omega_\mathrm{a} t_\mathrm{m}}{\left(\Omega_\mathrm{LO}^2 + \gamma^2\right)^2}, \end{aligned} \tag{D40}$$

where we have defined $\Gamma = \Gamma[\zeta/(\sqrt{2}\sigma)]$ with $\zeta = \gamma_2 + \gamma\Omega_\mathrm{C}^2/(\Omega_\mathrm{LO}^2 + \gamma^2)$ and $\sigma^2 = k_b T/m_R$. Moreover, we have introduced $\Gamma' = \partial_z \Gamma(z)\,|_{z \rightarrow \zeta/(\sqrt{2}\sigma)}$. Likewise, we can evaluate the variance for an ensemble of atoms

$$\langle \mathrm{Var}\hat{\mathcal{X}}\rangle = \langle\hat{\mathcal{X}}^2\rangle = \frac{4t_\mathrm{m}N}{\gamma_b + \frac{\omega_p\sigma}{c}\Gamma + \frac{\Omega_\mathrm{C}^2\gamma}{\Omega_\mathrm{LO}^2 + \gamma^2}}, \tag{D41}$$

where we have approximated the Rabi coupling between the Rydberg states by the local oscillator $\Omega \to \Omega_{\mathrm{LO}}$. Putting everything together, the SNR reads

$$\mathrm{SNR} \equiv \frac{\delta\langle\hat{\mathcal{X}}\rangle}{\langle \mathrm{Var}\hat{\mathcal{X}}\rangle^{\frac{1}{2}}} = \sqrt{N}\Omega_{\mathrm{a}}\sqrt{T_{\mathrm{c}}t_{\mathrm{m}}} = \sqrt{N}\Omega_{\mathrm{a}}\tau, \tag{D42}$$

where we have defined the effective measurement time $\tau = \sqrt{T_{\mathrm{c}}\, t_{\mathrm{m}}}$ in terms of the effective coherence time in Eq. (21). Finally, we recall that we have considered Ω as quasistatic throughout the derivations. Taking the time dependence $\Omega(t) = \Omega_{\mathrm{LO}} + \Omega_{\mathrm{a}} e^{i(\omega_{\mathrm{a}}-\omega_{\mathrm{LO}})t}$ into account, we find that the measurement signal will slowly oscillate with frequency $\omega_{\mathrm{a}} - \omega_{\mathrm{LO}}$ and amplitude in Eq. (D40). Thus, the SNR will remain unchanged in the case of heterodyning.

[1] B. Moore, Evidence against dissipation-less dark matter from observations of galaxy haloes, Nature (London) **370**, 629 (1994).

[2] M. Boylan-Kolchin, J. S. Bullock, and M. Kaplinghat, Too big to fail? The puzzling darkness of massive Milky Way subhaloes, Mon. Not. R. Astron. Soc. **415**, L40 (2011).

[3] G. Kauffmann, S. D. M. White, and B. Guiderdoni, The formation and evolution of galaxies within merging dark matter haloes., Mon. Not. R. Astron. Soc. **264**, 201 (1993).

[4] R. D. Peccei and H. R. Quinn, CP conservation in the presence of instantons, Phys. Rev. Lett. **38**, 1440 (1977).

[5] F. Wilczek, Problem of strong P and T invariance in the presence of instantons, Phys. Rev. Lett. **40**, 279 (1978).

[6] S. Weinberg, A new light boson? Phys. Rev. Lett. **40**, 223 (1978).

[7] F. Wilczek, Two applications of axion electrodynamics, Phys. Rev. Lett. **58**, 1799 (1987).

[8] L. Abbott and P. Sikivie, Cosmological bound on the invisible axion, Phys. Lett. B **120**, 133 (1983).

[9] M. Dine and W. Fischler, The not-so-harmless axion, Phys. Lett. B **120**, 137 (1983).

[10] J. Preskill, M. B. Wise, and F. Wilczek, Cosmology of the invisible axion, Phys. Lett. B **120**, 127 (1983).

[11] R. Li, J. Wang, X.-L. Qi, and S.-C. Zhang, Dynamical axion field in topological magnetic insulators, Nat. Phys. **6**, 284 (2010).

[12] D. M. Nenno, C. A. C. Garcia, J. Gooth, C. Felser, and P. Narang, Axion physics in condensed-matter systems, Nat. Rev. Phys. **2**, 682 (2020).

[13] J. Gooth *et al.*, Axionic charge-density wave in the Weyl semimetal $(\mathrm{TaSe}_4)_2\mathrm{I}$, Nature (London) **575**, 315 (2019).

[14] A. Sekine and K. Nomura, Axion electrodynamics in topological materials, J. Appl. Phys. **129**, 141101 (2021).

[15] L. Wu, M. Salehi, N. Koirala, J. Moon, S. Oh, and N. P. Armitage, Quantized Faraday and Kerr rotation and axion electrodynamics of a 3D topological insulator, Science **354**, 1124 (2016).

[16] Q. Li, D. E. Kharzeev, C. Zhang, Y. Huang, I. Pletikosic, A. V. Fedorov, R. D. Zhong, J. A. Schneeloch, G. D. Gu, and T. Valla, Observation of the chiral magnetic effect in ZrTe5, Nat. Phys. **12**, 550 (2016).

[17] M. Khlopov, A. Sakharov, and D. Sokoloff, The nonlinear modulation of the density distribution in standard axionic cdm and its cosmological impact, Nucl. Phys. B **72**, 105 (1999).

[18] V. Anastassopoulos *et al.* (CAST), New cast limit on the axion-photon interaction, Nat. Phys. **13**, 584 (2017).

[19] D. Noordhuis, A. Prabhu, S. J. Witte, A. Y. Chen, F. Cruz, and C. Weniger, Novel constraints on axions produced in pulsar polar-cap cascades, Phys. Rev. Lett. **131**, 111004 (2023).

[20] C. Boutan, M. Jones, B. H. LaRoque, N. S. Oblath, R. Cervantes, N. Du, N. Force, S. Kimes, R. Ottens, L. J. Rosenberg, G. Rybka, J. Yang, G. Carosi, N. Woollett, D. Bowring, A. S. Chou, R. Khatiwada, A. Sonnenschein, W. Wester, R. Bradley, E. Lentz *et al.* (ADMX Collaboration), Piezoelectrically tuned multimode cavity search for axion dark matter, Phys. Rev. Lett. **121**, 261302 (2018).

[21] C. Hagmann, P. Sikivie, N. S. Sullivan, and D. B. Tanner, Results from a search for cosmic axions, Phys. Rev. D **42**, 1297 (1990).

[22] M. Tada, Y. Kishimoto, K. Kominato, M. Shibata, H. Funahashi, K. Yamamoto, A. Masaike, and S. Matsuki, CARRACK II – a new large-scale experiment to search for axions with Rydberg-atom cavity detector, Nucl. Phys. B **72**, 164 (1999).

[23] B. M. Brubaker, L. Zhong, Y. V. Gurevich, S. B. Cahn, S. K. Lamoreaux, M. Simanovskaia, J. R. Root, S. M. Lewis, S. Al Kenany, K. M. Backes, I. Urdinaran, N. M. Rapidis, T. M. Shokair, K. A. van Bibber, D. A. Palken, M. Malnou, W. F. Kindel, M. A. Anil, K. W. Lehnert, and G. Carosi, First results from a microwave cavity axion search at 24 μeV, Phys. Rev. Lett. **118**, 061302 (2017).

[24] K. M. Backes *et al.* (HAYSTAC), A quantum-enhanced search for dark matter axions, Nature (London) **590**, 238 (2021).

[25] Y. Zhu, S. Ghosh, S. B. Cahn, M. J. Jewell, D. H. Speller, and R. H. Maruyama, Electromagnetically-induced-transparency spectroscopy of high-lying Rydberg states in $^{39}\mathrm{K}$, Phys. Rev. A **105**, 042808 (2022).

[26] M. A. Fedderke, P. W. Graham, and S. Rajendran, Axion dark matter detection with CMB polarization, Phys. Rev. D **100**, 015040 (2019).

[27] P. A. R. Ade, Z. Ahmed, M. Amiri, D. Barkats, R. Basu Thakur, C. A. Bischoff, D. Beck, J. J. Bock, H. Boenish, E. Bullock, V. Buza, J. R. Cheshire, J. Connors, J. Cornelison, M. Crumrine, A. Cukierman, E. V. Denison, M. Dierickx, L. Duband, M. Eiben, S. Zhang *et al.* (BICEP/Keck Collaboration), Bicep/*keck* xiv: Improved constraints on axionlike polarization oscillations in the cosmic microwave background, Phys. Rev. D **105**, 022006 (2022).

[28] J. W. Foster, Y. Kahn, O. Macias, Z. Sun, R. P. Eatough, V. I. Kondratiev, W. M. Peters, C. Weniger, and B. R. Safdi, Green bank and Effelsberg radio telescope searches for axion dark matter conversion in neutron star magnetospheres, Phys. Rev. Lett. **125**, 171301 (2020).

[29] B. R. Safdi, Z. Sun, and A. Y. Chen, Detecting axion dark matter with radio lines from neutron star populations, Phys. Rev. D **99**, 123021 (2019).
[30] E. Todarello, M. Regis, M. Taoso, M. Giannotti, J. Ruz, and J. K. Vogel, The Sun as a target for axion dark matter detection, arXiv:2312.13984.
[31] J. Sisk-Reynés, J. H. Matthews, C. S. Reynolds, H. R. Russell, R. N. Smith, and M. C. D. Marsh, New constraints on light axion-like particles using Chandra transmission grating spectroscopy of the powerful cluster-hosted quasar H1821+643, Mon. Not. R. Astron. Soc. **510**, 1264 (2021).
[32] D. Wouters and P. Brun, Constraints on axion-like particles from x-ray observations of the hydra galaxy cluster, Astrophys. J. **772**, 44 (2013).
[33] This list is by no means exhaustive, and we encourage the interested reader to consult [70] for a more comprehensive one.
[34] J. L. Ouellet, C. P. Salemi, J. W. Foster, R. Henning, Z. Bogorad, J. M. Conrad, J. A. Formaggio, Y. Kahn, J. Minervini, A. Radovinsky, N. L. Rodd, B. R. Safdi, J. Thaler, D. Winklehner, and L. Winslow, First results from ABRACADABRA-10 cm: A search for sub-μeV axion dark matter, Phys. Rev. Lett. **122**, 121802 (2019).
[35] N. Crisosto, P. Sikivie, N. S. Sullivan, D. B. Tanner, J. Yang, and G. Rybka, ADMX SLIC: Results from a superconducting LC circuit investigating cold axions, Phys. Rev. Lett. **124**, 241101 (2020).
[36] A. V. Gramolin, D. Aybas, D. Johnson, J. Adam, and A. O. Sushkov, Search for axion-like dark matter with ferromagnets, Nat. Phys. **17**, 79 (2021).
[37] A. Berlin, R. T. D'Agnolo, S. A. R. Ellis, and K. Zhou, Heterodyne broadband detection of axion dark matter, Phys. Rev. D **104**, L111701 (2021).
[38] M. E. Tobar, B. T. McAllister, and M. Goryachev, Poynting vector controversy in axion modified electrodynamics, Phys. Rev. D **105**, 045009 (2022).
[39] J. F. Bourhill, E. C. I. Paterson, M. Goryachev, and M. E. Tobar, Twisted anyon cavity resonators with bulk modes of chiral symmetry and sensitivity to ultra-light axion dark matter, Phys. Rev. D **108**, 052014 (2023).
[40] P. Sikivie, Experimental tests of the "invisible" axion, Phys. Rev. Lett. **51**, 1415 (1983).
[41] M. C. Huang and P. Sikivie, Structure of axionic domain walls, Phys. Rev. D **32**, 1560 (1985).
[42] R. Löw, H. Weimer, J. Nipper, J. B. Balewski, B. Butscher, H. P. Büchler, and T. Pfau, An experimental and theoretical guide to strongly interacting Rydberg gases, J. Phys. B **45**, 113001 (2012).
[43] C. L. Degen, F. Reinhard, and P. Cappellaro, Quantum sensing, Rev. Mod. Phys. **89**, 035002 (2017).
[44] M. Jing, Y. Hu, J. Ma, H. Zhang, L. Zhang, L. Xiao, and S. Jia, Atomic superheterodyne receiver based on microwave-dressed Rydberg spectroscopy, Nat. Phys. **16**, 911 (2020).
[45] C. Holloway, A. Artusio-Glimpse, M. Simons, N. Prajapati, and A. Robinson, Electromagnetically induced transparency, AVS Quantum Sci. **4**, 034401 (2022).
[46] B. Liu, L.-H. Zhang, Z.-K. Liu, Z.-Y. Zhang, Z.-H. Zhu, W. Gao, G.-C. Guo, D.-S. Ding, and B.-S. Shi, Highly sensitive measurement of a megahertz rf electric field with a Rydberg-atom sensor, Phys. Rev. Appl. **18**, 014045 (2022).
[47] K. C. Cox, D. H. Meyer, F. K. Fatemi, and P. D. Kunz, Quantum-limited atomic receiver in the electrically small regime, Phys. Rev. Lett. **121**, 110502 (2018).
[48] D. H. Meyer, Z. A. Castillo, K. C. Cox, and P. D. Kunz, Assessment of Rydberg atoms for wideband electric field sensing, J. Phys. B **53**, 034001 (2020).
[49] S. Mukamel, *Principles of Nonlinear Optical Spectroscopy* (Oxford University Press, Oxford, 1995).
[50] E. A. Power and S. Zienau, On the radiative contributions to the van der Waals force, Nuovo Cim. **6**, 7 (1957).
[51] A. H. Guth, M. P. Hertzberg, and C. Prescod-Weinstein, Do dark matter axions form a condensate with long-range correlation? Phys. Rev. D **92**, 103513 (2015).
[52] J. W. Foster, N. L. Rodd, and B. R. Safdi, Revealing the dark matter halo with axion direct detection, Phys. Rev. D **97**, 123006 (2018).
[53] M. Lisanti, M. Moschella, and W. Terrano, Stochastic properties of ultralight scalar field gradients, Phys. Rev. D **104**, 055037 (2021).
[54] M. O. Scully and M. S. Zubairy, *Quantum Optics* (Cambridge University Press, Cambridge, 1997).
[55] M. Fleischhauer, A. Imamoglu, and J. P. Marangos, Electromagnetically induced transparency: Optics in coherent media, Rev. Mod. Phys. **77**, 633 (2005).
[56] E. Robertson, N. Šibalić, R. Potvliege, and M. Jones, Arc 3.0: An expanded python toolbox for atomic physics calculations, Comput. Phys. Commun. **261**, 107814 (2021).
[57] G. Wang, Y.-X. Liu, J. M. Schloss, S. T. Alsid, D. A. Braje, and P. Cappellaro, Sensing of arbitrary-frequency fields using a quantum mixer, Phys. Rev. X **12**, 021061 (2022).
[58] A. Kumar, A. Suleymanzade, M. Stone, L. Taneja, A. Anferov, D. I. Schuster, and J. Simon, Quantum-enabled millimetre wave to optical transduction using neutral atoms, Nature (London) **615**, 614 (2023).
[59] S. Borówka, U. Pylypenko, M. Mazelanik, and M. Parniak, Continuous wideband microwave-to-optical converter based on room-temperature Rydberg atoms, Nat. Photon. **18**, 32 (2023).
[60] A. Mitridate, T. Trickle, Z. Zhang, and K. M. Zurek, Detectability of axion dark matter with phonon polaritons and magnons, Phys. Rev. D **102**, 095005 (2020).
[61] K. Yamamoto and S. Matsuki, Quantum analysis of the Rydberg atom cavity detector of dark matter axions, Nucl. Phys. B **72**, 132 (1999).
[62] S. Matsuki and K. Yamamoto, Direct detection of galactic axions with Rydberg atoms in an inhibited cavity regime, Phys. Lett. B **263**, 523 (1991).
[63] P. Sikivie, Axion dark matter detection using atomic transitions, Phys. Rev. Lett. **113**, 201301 (2014).
[64] V. Flambaum, H. B. Tran Tan, I. Samsonov, Y. Stadnik, and D. Budker, Resonant detection and production of axions with atoms, Int. J. Mod. Phys. A **33**, 1844030 (2018).
[65] K. Beloy *et al.* [Boulder Atomic Clock Optical Network (BACON) Collaboration], Frequency ratio measurements with 18-digit accuracy using a network of optical clocks, Nature (London) **591**, 564 (2021).

[66] G. Engelhardt, S. Choudhury, and W. V. Liu, Unified light-matter Floquet theory and its application to quantum communication, Phys. Rev. Res. **6**, 013116 (2024).

[67] K. A. Gilmore, M. Affolter, R. J. Lewis-Swan, D. Barberena, E. Jordan, A. M. Rey, and J. J. Bollinger, Quantum-enhanced sensing of displacements and electric fields with two-dimensional trapped-ion crystals, Science **373**, 673 (2021).

[68] D. Bluvstein, H. Levine, G. Semeghini, T. T. Wang, S. Ebadi, M. Kalinowski, A. Keesling, N. Maskara, H. Pichler, M. Greiner, V. Vuletić, and M. D. Lukin, A quantum processor based on coherent transport of entangled atom arrays, Nature (London) **604**, 451 (2022).

[69] E. N. Economou, *Green's Functions in Quantum Physics*, 3rd ed. (Springer, New York, 2006).

[70] C. O'Hare, cajohare/axionlimits: Axionlimits (2020).